1-1-2015

A Numerical Study Investigating Sensitivity of Radar Wave Propagation to the Marine Atmospheric Boundary Layer Environment

Nathan E. Lentini
Coastal Carolina University

A NUMERICAL STUDY INVESTIGATING SENSITIVITY OF RADAR WAVE PROPAGATION TO THE MARINE ATMOSPHERIC BOUNDARY LAYER ENVIRONMENT

By

Nathan E. Lentini

Submitted in Partial Fulfillment of the

Requirements for the Degree of Master of Science in

Coastal Marine and Wetland Studies in the

School of Coastal and Marine Systems Science

Coastal Carolina University

2015

Dr. Erin E. Hackett, Major Professor

Dr. Var Limpasuvan

Dr. Rich Viso

Dr. Michael Roberts, Dean

Dr. Paul Gayes, SCMSS Director

I dedicate this thesis to my beloved mother, father, and whole family

Acknowledgements

I would like to thank my advisor, Dr. Erin Hackett, for her instrumental support, guidance, and assistance in completing this thesis research project. She helped me a great deal to acquire and sharpen numerous skills in completing this thesis. I thank my thesis advisory committee, Dr. Rich Viso, Dr. Var Limpasuvan, and Dr. Paul Gayes, for their support and valuable feedback. I am grateful to Frank Ryan for providing the VTRPE simulation and also to Program Officer Steven Russell and the Office of Naval Research for supporting this research and enabling my participation at a major conference, Grant N00014-13-1-0307. I am thankful to Nathan Grimes and John Saeger for their work on the "stacked" model of atmospheric refractivity. Thanks to the faculty and staff of Coastal Carolina University and School of Coastal and Marine Systems Science for providing facilities, support, and teaching opportunities. I also extend thanks to my fellow graduate students and friends, who provided moral and technical support throughout the years. Finally, I am ever grateful to my family for their constant love, support, and encouragement.

Abstract

Radar is a remote sensor that is useful in scientific and military applications. The environment affects the accuracy of radar measurements as well as the predictability of a radar system's performance. Because of the complexity of the dynamic processes occurring in the marine atmospheric boundary layer (MABL), which includes the lowermost troposphere and ocean surface, the impact of the environment on radar is intricate and difficult to assess. To better understand the relative importance of various aspects of the MABL environment on radar wave propagation, this study evaluates the sensitivity of radar wave propagation to the MABL environment using a global sensitivity analysis (SA) method, the extended Fourier amplitude sensitivity test (EFAST), and the Variable Terrain Radio Parabolic Equation (VTRPE) simulation, which calculates propagation power of radar waves in a wide variety of marine atmospheric conditions. A total of 16 environmental parameters are examined, 8 parameterizing the rough ocean surface, and 8 parameterizing the atmospheric vertical refractivity profiles. Radar frequencies of 3, 9, and 15 GHz are each simulated with horizontal (HH) and vertical (VV) polarization, resulting in sensitivity calculations for 6 different cases. The study is conducted for a domain of 1 km in altitude and 60 km in range using a low grazing angle generic air/sea surveillance radar.

The relative importance of the different parameters varied much more with frequency than polarization. The EFAST method takes into account parameter interactions, which are found to be significant and can be essential to correctly interpret the significance of a parameter. Results show that the atmospheric mixed layer parameters are most

important, particularly the height of the mixed layer. Overall, swell period is the most significant ocean surface parameter. However, sea directionality is also important at 3 GHz, and sea surface roughness and salinity are important at 9 and 15 GHz, respectively. Sensitivities to ocean surface parameters, except those related to directionality, become more prominent as radar frequency increases, and some sensitivity differences with respect to polarization occur regarding sea surface characteristics. Due to spatial variability of sensitivity throughout the domain, regional analysis is performed, using short (0-10 km), mid (10-30 km), and long (30-60 km) range, and low (0-200 m), mid (200-600 m), and high (600-1000 m) altitude divisions (9 regions). The most sensitive parameter in each low altitude region, from short to long range, is evaporation duct height and mixed layer height (mid and long range). The mixed layer height is the most sensitive parameter in all mid-altitude regions. At high altitude, the most sensitive parameter varies with frequency, except at short range where it is the mixed layer refractivity gradient (i.e., *M*-gradient). At mid-range, the most sensitive parameters are the inversion layer strength, mixed layer *M*-gradient, and mixed layer height for 3, 9, and 15 GHz respectively. At long range, the inversion strength is the most sensitive parameter at 3 GHz, while at 9 and 15 GHz it is the wind speed. These regional sensitivity results, along with those for the whole domain, can be used to determine which environmental parameters need to be specified with high accuracy when accounting for their effects on propagation for various radar systems and applications. This sensitivity information can also be used to help guide field measurements for simulation validation studies as it indicates what aspects of the environment need to be focused on for such experimental campaigns. Furthermore, these results provide

guidance on prioritization of environmental characterization in numerical weather prediction (NWP) and inversion studies (e.g., refractivity from clutter (RFC) studies), which are the two most common numerical methods currently used to address environmental effects on propagation. Additionally, the methodology presented in this study can be used and applied to similar problems that seek to understand the sensitivity to environmental effects on other remote sensors, such as infrared (IR), optical, and acoustic sensors.

Table of Contents

1.0 Introduction 1
2.0 Background 5
2.1 Antenna 6
2.2 Environment 8
2.2.1 Atmosphere 9
2.2.2 Ocean Surface 14
2.3 Sensitivity Analysis Methods 16
2.3.1 Sampling-based Methods 17
2.3.2 Variance-based Methods 18
2.4 Prior Research 22
2.4.1 Extension of Prior Research 31
3.0 Methods 40
3.1 EFAST 40
3.2 VTRPE Simulation 43
3.2.1 Ocean Surface and Atmosphere 44
3.3 Numerical Experiments 46
4.0 Results 52
4.1 Atmosphere 54
4.1.1 Evaporation Layer 56
4.1.2 Mixed Layer 58
4.1.3 Inversion Layer 61
4.1.4 Upper Layer 64
4.2 Ocean Surface 65
4.2.1 Dielectric Properties 66
4.2.2 Directionality 68
4.2.3 Surface Roughness 70
5.0 Conclusions 88
6.0 References 94

List of Figures

Figure 1: Dipole (red) and isotropic (green) antenna patterns from a source located at the origin (reproduced here from O'Donnell, 2007)……33

Figure 2: Parabolic radiation pattern produced by a dish antenna (reproduced here from Wolff, 2009)……...34

Figure 3: Cosecant squared radiation pattern with the radiation source at the origin. The vertical axis is height and the horizontal axis is range. The blue outline is the ideal depiction and the red outline is what can be expected in practice (reproduced here from Wolff, 2009)……...35

Figure 4: Classification of refractivity in the troposphere on radio waves……..……...36

Figure 5: Diagram showing refractivity profiles of all types of ducts, with refractivity in *M*-units as the horizontal axis and height as the vertical axis: (a) Evaporation duct, where h_d is the duct height; (b) Surface duct, where duct height is defined from the surface up to h_2; (c) Combination of surface duct with an evaporation layer, with duct heights of h_2 and h_d respectively; (d) Elevated duct, where duct height is defined by the distance between h_2 to the intersection with the *M*-profile, shown by the grey vertical dotted line (reproduced here from Karimian et al., 2011)……..…….37

Figure 6: Simulated propagation loss for a surface-based duct with evaporation layer (left), with evaporation duct height of 36 m and surface duct (top of inversion layer) at about 140 m, compared with *PL* for a standard atmosphere (right)…….……..…38

Figure 7: (a) Diagram showing multipath phenomenon; the direct and indirect signal paths are shown; (b) various types of clutter…….39

Figure 8: Example of uniform distribution for parameter *SST* (Eqn. 15)……49

Figure 9: Sample *M*-profile produced by the "stacked" model, showing parameters for each layer (Eqn. 25)……...50

Figure 10: Example *SI* distribution for the potential refractivity gradient, c_0…….…….51

Figure 11: Main order (*SI*, blue) and total order (*TSI*, yellow) sensitivity results averaged over the whole domain for 3, 9, and 15 GHz as denoted in each subfigure title; (a-c) are for HH polarization and (d-f) are for VV polarization. The error bars indicate the variability of the *SI* and *TSI* values over the domain…….…….……...75

Figure 12: Plot of parameter rank versus average *TSI* for all frequencies and polarizations. For each frequency, the HH case is plotted using the ranked order of parameters for the VV case. The VV case will therefore always decrease with increasing rank. Points where the HH results do not decrease with increasing rank indicate a difference in rank between HH and VV parameters for a given frequency……...76

Figure 13: Definition of regions (1-9), referred to as low, mid, or high range/altitude……..77

Figure 14: Illustration of the relationship between mixed layer height (solid arrow), inversion layer base height (dashed arrow), and the evaporation layer, which is defined based on the evaporation duct height (Eqn. 26)…….78

Figure 15: Normalized *TSI* by region of (a) z_d and (b) c_0 for 3, 9, and 15 GHz at HH and VV polarizations (see legend). Note a value of 1 on the vertical axis indicates the most influential parameter in that region……79

Figure 16: Normalized *SI* (a and b) and *TSI* (c and d) by region for mixed layer height and refractivity gradient…….80

Figure 17: *M*-profiles for the "gradual" (m_{ML}/m_{IL}=0.18) and "abrupt" (m_{ML}/m_{IL}=1.29) transition cases……...81

Figure 18: Normalized *SI* (a and b) and *TSI* (c and d) by region for inversion layer height and strength…….82

Figure 19: Normalized sensitivity by region of m_u for (a) *TSI* and (b) *SI*……....83

Figure 20: Normalized *TSI* by region for (a) salinity and (b) temperature, of the sea surface……84

Figure 21: Normalized *TSI* by region for (a) swell direction and (b) wind direction…..85

Figure 22: Normalized *TSI* by region for roughness parameters: (a) z_0, (b) H_s, (c) T_s, (d) Ω, and (e) U_{10}…….86

Figure 23: Normalized *SI* by region for roughness parameters: (a) U_{10}, (b) z_0, (c) T_s, and (d) H_s……..87

Figure 24: Chart illustrating the top atmospheric (light blue) and ocean surface (dark blue) parameter for each region at all frequencies, shown for HH polarization and ranked by *TSI*. If there is a discrepancy between polarizations, the VV value is also noted. The top overall parameter in each region is bold with an asterisk. Axes are not to scale…...93

List of Symbols and Acronyms

A, B: Fourier coefficients used in EFAST

ANOVA: Analysis of variance

c_0: Potential refractivity gradient

DOE: Design of experiments

E: Average conditional expectation of the output

e: Water vapor partial pressure

EFAST: Extended Fourier amplitude sensitivity test

EIRP: Equivalent isotropic radiated power

EM: Electro-magnetic

F: Pattern propagation factor

FAST: Fourier amplitude sensitivity test

GFPWE: Green's function parabolic wave equation

G_t: Transmitter gain

HH: Horizontal-transmit and horizontal-receive

h_{IL}: Inversion layer height

h_{ML}: Mixed layer height

H_s: Swell height

IR: Infrared

k: Number of input parameters

k_0: Vacuum wave number

M: Index of refraction in *M*-units (all chapters); number of harmonics (Ch. 3.0)

M_0: Refractivity at sea surface

MABL: Marine atmospheric boundary layer

MC: Monte Carlo

m_{ML}: Mixed layer refractivity gradient

m_U: Upper layer refractivity gradient

n: Index of refraction

N: Index of refraction in *N*-units (Ch. 2.0); number of samples (Ch. 3.0)

NCODA: Navy coupled ocean data assimilation

NWP: Numerical weather prediction

OAT: One at a time test

P: Pressure

PE: Parabolic equation

PF: Power pattern propagation factor

PL: Power pattern path loss

P_r: Power received

P_t: Power transmitted

R: Slant range

Radar: Radio detection and ranging

R_E: Radius of the earth

RF: Radio frequency

RFC: Refractivity from clutter

RH: Relative humidity

RMSE: Root mean square error

s: Frequency domain search variable used in FAST and EFAST

SA: Sensitivity analysis

SI: Sensitivity index

SSS: Sea surface salinity

SST: Sea surface temperature

T: Temperature

TE: Transverse electric

TM: Transverse magnetic

T_s: Swell period

TSI: Total sensitivity index

U_{10}: Wind speed at 10 m

V: Unconditional variance of output

V_{-i}: Partial variance of complementary parameter set

V_i: Partial variance of parameter *i*

VOCAR: Variability of coastal atmospheric refractivity

VTRPE: Variable Terrain Radio Parabolic Equation

VV: Vertical-transmit and vertical-receive

WS: Winding stairs

X_i: Input parameter

Y: Model output

z_0: Aerodynamic roughness height

z_1: Height to the base of the inversion layer

z_2: Height to the top of the inversion layer

z_d: Evaporation duct height

z_L: Evaporation layer height

ΔM: Inversion layer strength

ε: Dielectric constant of medium

ε_0: Dielectric constant of free space

ε_r: Relative dielectric constant

Θ_s: Swell direction

Θ_w: Wind direction

λ: Radar wavelength

φ_i: Random phase shift used in transformation function

Ω: Wave age

ω_i: Frequency assigned to parameter *i*

ω_{-i}: Frequency set assigned to complementary parameter set

ω_{max}: Maximum frequency

ω_{Ny}: Nyquist frequency

1.0 Introduction

Radar (radio detection and ranging) is an electronic system used to remotely sense position, direction, and/or speed of objects. The basic components of a radar system are the transmitter and receiver. The transmitter emits electromagnetic (EM) waves at radio frequency (RF), ranging from the order of 10^4 to 10^9 Hz (kHz to GHz), traveling at approximately the speed of light. Radar waves reflect off an object and travel back to the receiver. Properties of the reflected waves are then analyzed to infer appropriate properties of the object.

Radar is a powerful remote sensing tool and widely used sensor because of its ability to detect long range objects over very small time intervals. Applications of radar include military surveillance of air and sea, civilian air traffic, meteorological tracking, and other scientific applications. Some examples of meteorological and scientific uses of radar are the detection of storm, tornado, precipitation, and clouds, and the measurement of wind and waves. When using meteorological radar, the reading integrity of the size, density, and position of hydrometeors may be compromised (e.g., rain may be misread as hail) due to various sources of errors. Radar phenomenology encompasses radar cross section models, clutter, Doppler effects, and atmospheric/oceanic effects.

The accuracy of radar measurements can be impacted by noise and biases associated with system components or unknown affects due to the medium through which radar

waves propagate. Designers of radar often assume the propagation medium is a standard atmosphere and consequently radar specifications are usually based on these conditions. The MABL is an especially complex environment and can adversely affect propagation in the context of "instantaneous" measurements (e.g., any given day or hour). Determining the sensitivity of radar wave propagation to environmental parameters in the MABL enables one to better determine what aspects of the environment might significantly impact radar performance and consequently possible sources of deviation from expected standard atmospheric system performance/specifications.

It is often desirable to be able to predict how a radar system will perform in a particular environment. High-fidelity radar wave propagation codes can simulate the environmental effects on propagation. However, discrepancies between measured and predicted propagation often still exist, which are generally attributed to insufficient accuracy of the modeled environment (Sirkova, 2012). Thus, sensitivity information can also help prioritize which environmental factors are responsible for the most significant discrepancies when validating propagation models, and likewise, which aspects of the environment need to be measured at high accuracy for validation studies.

Because of the limitations (e.g., cost and logistics) in obtaining high-resolution meteorological data regarding "instantaneous" conditions, inversion techniques have become an increasingly popular way to estimate environmental conditions. Inversion approaches, such as RFC, determine environmental parameters from measured clutter and advanced propagation simulations (Gerstoft et al., 2003; Marshal et al., 2008; Karimian et al., 2011; Karimian et al., 2013). One of the limitations of any inversion problem is the number of parameters that can be inverted-for because as the number of parameters

increases the posedness of the inverse problem decreases. Thus, quantification of sensitivity can also be used to help solve these types of inversion problems because it reveals which parameters need to be solved for to obtain different levels of accuracy from the inversion.

For all the reasons outlined above, understanding the sensitivity of radar wave propagation to the MABL is useful knowledge towards improving our ability to understand and improve radar system performance in a variety of environments and radar system applications. The computation of sensitivity is complex because the MABL encompasses the lower atmosphere and the ocean surface, as well as all the associated air-sea interactions that couple these two regions. In the MABL, the atmosphere is turbulent and exchanges of heat and water content occur across the air-sea interface, and the sea surface is rough and non-stationary. The interactive nature of the environment combined with the numerous ways in which radar waves interact with this environment (e.g., refraction, diffraction, reflection, scattering) make this information challenging to obtain.

The goal of this study is to determine the sensitivity of radar wave propagation to the MABL environment, which is defined here as extending from the sea surface up to 1000 m in altitude. This study targets S, X, and Ku band systems at horizontal (HH) and vertical (VV) polarization and are simulated as ship-borne/platform-based air/sea surveillance radars at low grazing angles. The Variable Terrain Radio Parabolic Equation (VTRPE) simulation is used to simulate radar wave propagation in a complex marine-atmospheric environment. VTRPE accounts for a wide range of meteorological effects on radio wave propagation, such as refraction, attenuation, scattering, and

absorption. The Extended Fourier Amplitude Sensitivity Test (EFAST) method is used for the sensitivity analysis (SA).

The next section provides some background information on the effects of the environment on radar wave propagation as well as information on sensitivity analysis methods. The Methods section discusses the implementation of the EFAST method to this study, an overview of the VTRPE simulation, and the environmental parameters examined. Subsequently, the results of the SA are presented, and the thesis ends with a concluding chapter.

2.0 Background

The air molecules in the atmosphere, the marine surface, and coupled effects of both variable atmosphere and sea state impact radar propagation and can lead to anomalous propagation. Anomalous radar wave propagation is defined as any propagation behavior not observed in a standard atmosphere (global average), defined based on standard temperature, pressure, and humidity profiles. Meteorological phenomena that cause non-standard conditions include sea breezes, air mass subsidence, cloud layers, fronts, and atmospheric perturbations. Variation in the atmosphere's thermodynamic properties causes the index of refraction to vary, which impacts radar wave propagation. Refraction, attenuation, scattering, absorption, and other effects arise as a result of propagation in the earth's atmosphere above the sea surface, changing the radar signal strength and direction.

Radar propagation is generally characterized by the radar transmission equation (Friis, 1947; Freehafer et al., 1951):

$$\frac{P_r}{P_t} = G_t \left[\frac{F}{2k_0 R}\right]^2 , \tag{1}$$

which is the one-way transmission equation, from transmitter to target. Eqn. (1) gives the ratio of the power received by an omnidirectional receiver, P_r, to the power emitted from a transmitting antenna, P_t, where G_t is the transmitter peak power gain, R is the slant range (defined by a straight line from radar to target), and k_0 is the vacuum wavenumber:

$$k_0 = \frac{2\pi}{\lambda}, \tag{2}$$

where, λ is wavelength of the radar wave. In Eqn. (1), F is the one-way pattern propagation factor from transmitter to target. Eqn. (1) assumes that the polarization is the same for the transmitted and received radio waves. The power transmitted, P_t, is the equivalent isotropic radiated power (EIRP), which means radiated uniformly in all directions. The pattern propagation factor, F, accounts for environmental effects on radar wave propagation. The complex pattern propagation factor, $\boldsymbol{F}$, can now be introduced as:

$$\boldsymbol{F} = \frac{\boldsymbol{E}}{\boldsymbol{E_0}}, \tag{3}$$

defined as the ratio of the electric field, $\boldsymbol{E}$, to the electric field in free-space, $\boldsymbol{E_0}$. The magnitude of $\boldsymbol{F}$ is equal to the pattern propagation factor, F. Because the range of F is large, it is converted to decibel units (dB):

$$PF = 20\log|F| \tag{4}$$

$$PL = 20\log(2k_0R) - 20\log|F| \tag{5}$$

The variables PF and PL are known as the power pattern propagation factor and the power pattern path loss, respectively, and are measures of power. The power pattern path loss is equal to the PF in free space minus the PF in the environment.

2.1 Antenna

The primary components of radar are the transmitter, duplexer, receiver, antenna, and display. The antenna can be part of the transmitting apparatus or a separate device. A

radar system can be classified as mono-static or bi-static. A mono-static system has the transmitter and receiver in the same location; a bi-static system has the transmitter and receiver in different locations.

In a mono-static system, the duplexer allows one antenna to function as a transmitter and a receiver. By switching between the two communication modes, the duplexer protects the receiver from the high-power pulses of the transmitter. The electronics inside the transmitter apparatus are made up of sub-components, such as filters, pulse width modulators, cathode ray A/R-scopes, and amplifiers. Technologically advanced transmitter designs permit control over several characteristics of the generated EM waves, such as polarization and frequency. The directivity of the radar wave (i.e., the antenna pattern) can also be shaped.

The basic characteristics of antennas are gain, pattern, beam width, side lobe number and intensity, front-to-back ratio, and aperture (Wolff, 2009). The intended use of the antenna dictates its design. Despite the variety of physical design, antennae typically fall into 2 categories: directional and non-directional. The classic non-directional antenna pattern is isotropic, radiating in all directions with equal intensity (i.e., a true point source). However, true isotropic radiation is not practical to achieve. Therefore, omni-directional is the term used to describe the pattern, as a more realistic reference to uniform propagation in all directions. An omni-directional pattern is commonly generated from a point dipole source and resembles a donut shape. Figure 1 illustrates the difference between an omnidirectional dipole (more practical) and an isotropic antenna pattern (O'Donnell, 2007).

The parabolic dish design is commonly used as a directional antenna. The circular parabolic reflector concentrates the beam rays at the focal point of the concave dish. An ideal parabolic reflector is completely circular and produces a narrow 'pencil' beam, similar to what is shown in Figure 2 (Wolff, 2009). An elliptical dish produces a fan beam, which is less intense and has greater beam width.

Examples of more complex patterns are the cosine squared and cosecant squared patterns, named for the relationship between vertical angle and coverage of the radar beam. These patterns provide greater coverage than simple "pencil" or "fan" beam shapes. The cosine squared pattern is more mathematically canonical than practical. The cosecant squared beam pattern is more complex and more commonly used in practice because the shape gives greater altitude coverage at short range than cosine squared. The cosecant squared pattern is shown in Figure 3 (Wolff, 2009). Cosecant squared patterns are effective for air surveillance applications. The 'look angle' can be changed from 'look up' (shown in Figure 3) to 'look down.' A reflection of the image in Figure 3 about the horizontal axis would be a 'look down' pattern, which is effective for sea surface surveillance.

2.2 Environment

The environmental effects on radar wave propagation in the MABL environment can be divided into those due to the atmosphere and those due to the ocean surface. However, it is important to note that the atmosphere and ocean surface interact as a coupled system. Atmospheric effects on propagating EM waves include refraction, attenuation, and absorption. Ocean surface effects include scattering and absorption.

2.2.1 Atmosphere

Refraction describes the bending of radio waves as they propagate. Refraction is measured by the index of refraction, which is a property of the medium. Free space (e.g., vacuum) has an index of refraction of 1 (minimum value); all other media have indices of refraction higher than 1. The index of refraction is directly related to the dielectric nature of the medium. The dielectric nature is measured by the dielectric constant, which quantifies how easily matter becomes polarized in an electric field.

The relationship between the index of refraction, n, and relative dielectric constant, ε_r, is given by:

$$n = \sqrt{\varepsilon_r}\,, \tag{6}$$

where,

$$\varepsilon_r = \frac{\varepsilon}{\varepsilon_0} \tag{7}$$

ε is the dielectric constant of the medium, and ε_0 is the dielectric constant of free space. The earth's atmosphere can be divided into layers. The troposphere is nearest to the earth's surface, and extends from the surface to 8-15 km above sea level (depending on latitudinal location). The MABL is a sub-layer within the troposphere that is closest to the surface, extending 1 to 2 km above sea level. In the MABL, the index of refraction varies significantly because the MABL is turbulent and is a manifestation of complex air-sea interaction, such as moisture and heat exchange. Even so, the index of refraction, n, is only slightly greater than 1, and varies maximally on the order of ten-thousandths.

However, minute variation of *n* can have profound effects on radar wave propagation. To make n more convenient to work with, *N*-units are introduced, expressed by:

$$N = (n - 1) \times 10^6 \tag{8}$$

Thus, N is a measure of the difference between the atmosphere's index of refraction and that of free space ($n_0 = 1$), multiplied by 10^6. Changes in *N* are caused primarily by variations in temperature, *T*, and water vapor in the air. Water vapor content is measured by relative humidity, *RH*, or partial water vapor pressure, *e*. The water vapor content and temperature generally vary more rapidly with altitude than (horizontal) range. Pressure, *P*, varies with altitude and range and generally has a relatively small effect on *N*. The empirical relation between *N* and *T*, *P*, and *e* is given by Bean and Dutton (1968):

$$N = 77.6\frac{P}{T} + 373{,}256\frac{e}{T^2} \tag{9}$$

The refractive condition of the atmosphere is classified into 4 main categories: standard, sub-refractive, super-refractive, and ducting conditions. In a standard atmosphere, the EM waves diverge slightly from the earth. In a sub-refractive environment, the radar rays diverge away from the earth even more rapidly. In a super-refractive environment, the rays bend toward the earth more so than in a standard atmosphere, but still diverge from the earth. In a special condition called ducting, the rays bend enough to converge toward the earth surface. These refractive conditions are illustrated in Figure 4.

Modified refractivity (measured in *M*-units) is introduced specifically to account for the curvature of the earth and identify ducting conditions, defined as:

$$M = N + \frac{1}{R_e}(10^6)z\ , \tag{10}$$

where, R_e is the radius of the earth and z is altitude. This representation of refractivity is especially useful in identifying ducting because ducting occurs when the *M*-gradient is negative. Ducting can arise from complex meteorological conditions, which leads to one or more of 3 main duct types: evaporation, surface, and elevated ducts. The vertical refractivity profiles associated with these different ducts are shown in Figure 5.

According to Turton et al. (1988), all ducts are generally formed by a strong hydrolapse (rapid change in moisture with height) or temperature inversion, where temperature increases with height. The meteorological processes that bring about these conditions are: evaporation over the sea, anticyclonic subsidence, subsidence at frontal surfaces, nocturnal radiative cooling over land, and advection. Evaporation ducts, which are the most prevalent in the marine-atmospheric environment (Skolnik, 1990), form as a result of strong humidity gradients near the water surface. Evaporation ducts are found at low altitude, usually within 50 m of the surface. Surface ducts are typically created by temperature inversions. In the MABL environment, they are usually created by advection of warm dry air masses from land over cool humid marine surfaces. Rapid rates of heat transfer and humidification cause a stable layer of cool air to form near the surface with warm drier air above it (Karimian et al., 2011). Figure 6 shows VTRPE simulated propagation loss (*PL*) in the presence of both a surface and an evaporation duct over a smooth sea surface compared with that of a standard atmosphere. The trapping, or ducting, behavior is visible at the lower altitudes. Elevated ducts are similar to surface ducts, except that they occur at higher altitudes, and their height is not measured from the sea surface. Because of the complex nature of MABL conditions, ducting can be difficult to predict accurately. The refractivity structure also provides a basis for the layering of

the MABL. It can be roughly divided into an evaporation layer, mixed layer, inversion layer, and upper layer. The evaporation and inversion layers are where ducts may exist and the mixed and upper layers are where constant non-ducting refractivity gradients exist. Obviously, the heights and refractivity gradients of each layer vary, and some layers are not present at times (i.e. ducting layers). An *M*-profile with all layers present would look similar to Figure 5c.

In addition to refraction, attenuation also affects signal propagation. Attenuation is the reduction of EM signal power along a propagation path (Battan, 1973). Absorption and scattering are the two main mechanisms by which attenuation occurs. Attenuation can be expressed by coefficients that account for absorptive and scattering effects, either cumulatively in one attenuation coefficient or individually in absorption and scattering coefficients that are additive. The attenuation coefficient has the same form as the extinction coefficient in optics, and has units of reciprocal length (i.e., m^{-1} or km^{-1}) because it is an intensity gradient that varies with length. The coefficients can also be categorized by meteorological cause: gases, clouds, and precipitation. Attenuation is dependent on frequency (wavelength) and particle size. In general, higher frequency (shorter wavelength) signals experience more attenuation, and are more significantly affected by gas, clouds, aerosols, and precipitation. Lower frequency (longer wavelength) signals are affected by clouds and precipitation, but not as much by gas, which is likely due in part to different scattering mechanisms. Rayleigh scattering occurs when the particles are small (ratio of circumference-to-wavelength is less than 0.2); if particles are larger, Mie scattering occurs, which can affect the energy of the scattered radar wave (Falcone, Jr. and Dyer, 1985).

The atmospheric gases that contribute most to attenuation are water vapor and oxygen. The reason is that these molecules behave like strong electromagnetic dipoles when interacting with EM waves, consisting of an alternating electric field and an orthogonal magnetic field. Water vapor has a dipole moment due to the electric field and oxygen has a dipole moment due to the magnetic field. Each gas molecule has a positive and negative pole. Molecules with dipoles are referred to as polarized. "Dipole moment" is the measure of strength of polarization. Research on attenuation due to atmospheric gases has been carried out by Van Vleck (1947a) and Bean & Dutton (1968), particularly on EM signals with wavelengths of about 1 cm travelling long range. The incident EM wave causes molecular vibrations and rotations in many directions, transferring energy to the gas molecule. Some of this energy is absorbed, increasing the energy level of the gas molecule, and some is scattered randomly. Because all energy gained by the gas molecule comes from the incident wave, the outgoing wave has lower energy than that encountered by the gas molecule. The frequency dependence of attenuation reflects the resonant behavior of the interacting substance and its natural (resonant) frequency. According to Van Vleck (1947b), water vapor has two resonant frequencies (wavelengths) at 22.235 GHz (1.35 cm) and 150 GHz (0.2 cm); oxygen has one resonant frequency (wavelength) at 60 GHz (0.5 cm). In studying attenuation effects (especially scattering), the resonant property of a material is often expressed as wavelength for comparison to the particle dimension. Because of their high frequency and resonant phenomena, K-band radars are sensitive to attenuation. Bean & Dutton (1968) examined the gaseous absorption dependence on pressure and temperature. It was shown that signal wavelengths in the millimeter range are subject to a high magnitude of gaseous

attenuation, and wavelengths greater than 3 cm have negligible gaseous attenuation (Bean & Dutton, 1968).

In general, liquid causes higher attenuation rates than gas. Therefore, more attenuation occurs in rainy environments than with gases alone. Gunn & East (1954) determined theoretical relations for precipitation attenuation coefficients and compared them to numerous experimental results; the relations can be used for various types of precipitation, including rain and snow. Snow is a special case of precipitation, which causes more attenuation when wet (e.g., graupel).

Clouds exhibit less attenuation intensity than rain, but occur more regularly. Signal weakening due to clouds is primarily from absorptive losses. The magnitude of attenuation depends on the cloud liquid water content, and is likely also influenced by cloud thickness to some degree. The cloud attenuation constant is a function of signal frequency and temperature.

2.2.2 Ocean Surface

Signal power is affected by the ocean surface mainly through scattering and absorption mechanisms. Power loss occurs due to the incident signal splitting into transmitted and reflected component waveforms. The reflected ray is weaker than the incident ray and has a different phase. Ray transmission is an absorptive effect. Ray reflection is a scattering effect. For reflected rays, the direction of propagation is important, because some rays may scatter away from the receiver.

Multipath is a radar phenomenon that occurs when radar waves take different paths between the transmitter, target, and receiver, shown in Figure 7a. Some rays take the

direct path, and some take an indirect path by reflecting off the sea surface. Constructive and destructive interference between a signal on the direct path and a signal on an indirect path can modulate the received signal. For a horizontally polarized beam over a smooth surface, one-way multipath usually shows modulations (gain and loss) of roughly 6 dB and two-way multipath modulations are normally about 12 dB. For the case of oblique incidence on a smooth boundary, the reflected wave is phase shifted and scaled up in amplitude (Griffiths, 1998). However, the sea surface is not smooth, and consequently the effects of multipath are not well understood. Furthermore, the rough surface affects the reflection coefficient from the surface in addition to incoherent scattering from the surface. Received signals from the ocean surface are called sea clutter, illustrated in Figure 7b, along with other types of clutter.

In addition, exchange of water vapor and heat across the air-sea interface impacts the atmospheric index of refraction near the sea surface, as discussed in *2.2.1*. Breaking waves lead to the injection of aerosols, such as sea spray and salt, into the atmosphere, which have an impact on refraction and attenuation. The sea surface salinity and temperature affect the dielectric properties of the sea water, which in turn have an impact on refractivity and reflectivity of the sea surface. The directionality of the wind and ocean waves, along with factors like wave height, wave period, and wind speed, also play a role in shaping the rough sea surface. The rough ocean surface introduces significant complexities in propagation behavior and makes propagation prediction considerably more challenging.

2.3 Sensitivity Analysis Methods

In order to evaluate the sensitivity of radar wave propagation to the environmental effects described in the previous section, a methodology for the sensitivity analysis must be determined. In this section, various types of sensitivity analysis methods are discussed and compared. The methods can be classified as sampling or variance based; they can also be categorized as local or global. A local method does not account for interaction effects between parameters, whereas a global method does. Some of the methods can be categorized as *screening methods*, whose purpose is to narrow down which input parameters are most influential on a model output.

The primary screening method is the one-at-a-time (OAT) method. OAT is a local perturbation approach, where one input factor is varied over a range while all other parameters are fixed at a nominal value, and the impact on the output is computed. OAT is a commonly used SA technique because of its ease of implementation. One important drawback is that interaction effects between parameters are not included. Thus, any significant coupled effects between parameters are ignored in the assessment. The advantage of the OAT method is that it is computationally cheap and has relatively quick execution time. It can be useful for studies with many input factors when it is desirable to filter the parameter list down to the most significant group.

In order to account for coupled effects, parameter combinations can be varied, such as done in the Morris Method (Ekstrom, 2005). The Morris method is a variation of the OAT method with the improvement of being qualitatively global. The Morris method is an experimental plan made up of individually randomized OAT designs. It uses a factorial sampling plan as part of a screening method in computational experiments

(Morris, 1991). The Morris method fits into a category of sensitivity analysis called design of experiments (DOE).

2.3.1 Sampling-based Methods

Sampling based SA methods are commonly used, and can be local or global. To calculate sensitivity, sampling based methods use a Monte Carlo (MC) approach to map the relationship between input and output. Sampling based methods include graphical methods, regression analysis, correlation coefficients, rank transformations, and 2-sample tests. Graphical methods are simple ways of visualizing the relationship between input and output factors. A scatter plot is an example of a graphical approach, and is most effective for simple models where only a few input factors and one output exist (Ekstrom, 2005). Regression analysis is a method that fits the input-output data to a theoretical equation with minimal error. Regression can be applied to all models with multiple inputs and one output, but is most effective as a sensitivity analysis tool for linear models.

A sampling based method that can be applied to non-linear models is the rank transformation method, named because it has the ability to transform a non-linear model into a linear one. However, the model must be monotonic so that the input is directly related to the output. A rank transformation assigns a rank to each parameter, which is then used in a regression or correlation analysis in place of the data to calculate rank coefficients.

2.3.2 Variance-based Methods

Variance based methods are more complex in their execution than sampling based methods, but are better suited for complex models. The variance that each input factor, X_i, contributes to the output, *Y*, is quantified. Thus, the level of influence of each input's variance on the unconditional variance of the output can be quantified. In order to compute this quantity, the average conditional variance of *Y* for an input factor X_i is calculated, known as the expectation value of the output over the entire input interval. The variance of the average conditional expectation, $V(E[Y|X_i])$, and unconditional variance of the output, $V(Y)$, are used to define the 1st order sensitivity index, *SI* (Saltelli et al., 1999), as:

$$SI = \frac{V(E[Y|X_i])}{V(Y)} \tag{11}$$

The 1st order *SI* only accounts for the leading order effect of the input factor on the output. Higher order interaction effects with other inputs are not accounted for by this *SI*. A first order *SI* value can be between zero and one, with zero indicating no effect and one indicating responsibility for the total variation of the output. If the sum of all first order *SI*'s equals one, the model is additive (i.e., linear). If the model is non-additive (i.e., non-linear), interactions exist between inputs. For example, interaction effects exist for two input factors if the sum of their leading order sensitivity indices does not equal the total effect on the output. Interactions are quantified by higher order *SI*'s. The total effect of an input factor on the output is the sum of both the leading and higher order sensitivity indices, called the total sensitivity index, *TSI* (Saltelli et al., 2000). For example, in a 3-input model, the *TSI* for the first input is:

$$TSI_1 = SI_1 + SI_{12} + SI_{13} + SI_{123}\,, \tag{12}$$

where SI_1 is the 1st order *SI* for input 1, SI_{12} and SI_{13} are 2nd order *SI*'s that account for interactions between inputs 1 & 2 and 1 & 3 respectively, and S_{123} is the 3rd order interaction *SI* between inputs 1, 2, and 3 (Ekstrom, 2005). The primary variance based methods are the Design of Experiments (DOE), the Sobol method, Jansen's Winding Stairs (WS), the Fourier Amplitude Sensitivity Test (FAST), and the Extended Fourier Amplitude Sensitivity Test (EFAST).

DOE methods are among the first variance based methods to be used in sensitivity analysis, utilizing statistics such as the expectation and variance. Recall that the expectation is the output value expected, conditional on a fixed value of an input. The variance of the output is computed over the full range of values for the input. This output variance due to variation of an input is a measure of sensitivity. Interaction effects can also be calculated by decomposing the variance into partial variances of increasing dimensionality, as performed in an analysis of variance (ANOVA), where variance of a single variable is apportioned into components attributable to different sources of variation. A dimension is the order of effect; higher order effects account for interactions of increasing complexity (i.e., 1st order →main effect, 2nd order → 2-way interaction, nth order → n-way interaction). FAST and Sobol indices are ANOVA-like in that they utilize variance decompositions to calculate sensitivity indices. The Sobol method is an extension of DOE into numerical experiments. A paradox arises when comparing DOE on physical versus numerical experiments. The original intended use for DOE is for physical experiments, where input parameters are usually varied over a small range for practical reasons. Interaction effects can be typically calculated for physical experiments

using DOE for this reason. Numerical studies, on the other hand, typically vary input parameters over a large range, making it much more difficult to calculate higher order effects. The number of simulation runs for DOE including interaction effects for a large number of input parameters (e.g., more than 5) becomes a limiting factor for its implementation.

The method of Sobol indices is one of the first to utilize the 1st order sensitivity index (Sobol, 1993). The total variance $V(Y)$ is computed by an integral over the whole parameter space, known as the unit hypercube. The partial variance for parameter *i* is V_i $(1 \leq i \leq k)$, where k is the number of input parameters. The partial variance is computed for all parameters, thereby discerning the source of variation due to that parameter.

MC methods can be used to calculate the integrals necessary to get the total variance and partial variances. The 1st order sensitivity index is then defined as the ratio of the partial variance of an input parameter to the total variance:

$$SI_1 = \frac{V_1}{V(Y)} \tag{13}$$

Because it is normalized, the *SI* value is between 0 and 1. As stated earlier, if the primary (1st order) *SI*'s for all parameters do not add up to 1, interaction (higher order) effects must be present, and *TSI* calculation is necessary to quantify the total effect of a parameter. The Sobol method can calculate the *TSI* (Sobol, 2001). Though the Sobol method is global, it is somewhat expensive computationally. For k input factors and N samples of each parameter, $N(2k + 1)$ model evaluations are required.

The WS method is another variance-based method proposed by Jansen et al. (1994). The WS method is used to measure the main effect (*SI*) and total effect (*TSI*) with one series of model evaluations. Therefore, Jansen's WS method is more efficient in making use of model evaluations. WS works by building a matrix, named the WS-matrix, made up of output values that are functions of a group of input parameters. The variance and MC variance are computed from the WS-matrix, which are used to calculate the main and total effect. A key difference between the Sobol and Jansen methods is that the Sobol method uses the product of model outputs, and Jansen's method uses the squared difference, to calculate the sensitivity indices.

The FAST method operates on the principle that the input parameter space can be explored by transforming a *k*-dimensional parameter space into a 1-dimensional space using a search variable (Saltelli et al., 2000). For a model, *k* dimensions correspond to *k* input parameters. The FAST method offers a way to collapse all those variables into one variable. This reduction is accomplished using a transformation function. Before the transformation function can be applied, however, all variables are assigned a frequency. Two requirements must be met to carry out FAST analysis accurately: 1) The input parameters must be independent of each other, and 2) the assigned frequencies must be incommensurate, meaning no two frequencies are linearly dependent. A given parameter's frequency is used in a sinusoidal transformation function that converts the parameter to *s*-space (frequency domain).

For a given parameter frequency, the search variable, *s*, is spanned over one cycle (2π radians), which ensures the entire parameter space is covered. The model outputs can be expanded into a Fourier series. Because the frequencies are incommensurate, Fourier

coefficients that correspond to an input parameter's frequency and harmonics are only affected by the parameter under investigation. The frequencies that produce the greatest amplitude response of the output reveal that the model output is most sensitive to the parameters associated with those frequencies. In order to quantify this, the *SI* and, in the extended version of FAST (Saltelli et al., 1999), the *TSI* is calculated. These sensitivity indices are calculated from the partial and total variance.

The extended Fourier amplitude sensitivity test (EFAST) is a generalized version of the classic FAST method (Cukier et al., 1973; Schaibly and Shuler, 1973; Cukier et al., 1975; Cukier et al., 1978). EFAST offers increased robustness and computational efficiency (Saltelli et al., 1999, 2000; Koda et al., 1979), by allowing a lower sample size to be used to perform sensitivity calculations (i.e., fewer simulation runs). The most valuable improvement is the ability to calculate *TSI* as well as *SI*, where the former accounts for interactions between parameters. The method is well suited for non-linear and non-additive models while requiring fewer simulation runs. Because of the complexity (e.g., likely that coupled effects are significant), large number of inputs, and nontrivial runtime of the VTRPE radar wave propagation simulation, the EFAST method is appropriate for this study and its implementation is discussed in detail in the Methods section.

2.4 Prior Research

There have been numerous studies that examine the effects of the troposphere and sea surface on radar propagation, both experimentally and numerically (Stephansen, 1981; Hitney et al., 1985). For the numerical studies, one of the most recent and promising methods is parabolic equation (PE) modeling of EM wave propagation, reviewed by Sirkova (2012) and described in the context of assessing radar performance by Craig and

Levy (1991). Most experimental and numerical studies specifically focus on a few aspects of the lower troposphere, such as the evaporation duct or surface roughness.

Evaporation ducting has been extensively studied, empirically and numerically, mainly because it is the most common type of ducting in the marine environment (Turton et al., 1988). A common effect of evaporation ducts on propagation is enhanced range performance of the radar (Anderson, 1989), which is why knowledge of the presence of a duct is important. However, some studies have shown that lower average power can occur in the duct (and higher amplitude random power variation above the duct) due to leakage of energy from the duct (Kukushkin, 2004). This leakage has been attributed to scattering of EM waves from turbulent fluctuations of the refractive index (Ivanov et al., 2009). Some of these discrepancies are due to different studies being conducted at different radar frequencies as the impact of the duct on propagation is frequency dependent (Hitney and Hitney, 1990; Hitney and Veith, 1990). The most commonly examined parameter associated with the evaporation duct is the duct height, z_d (Kerr, 1951; Turton et al., 1988; Anderson, 1989; Paulus, 1990; Sirkova and Mikhalev, 2003), defined as the height where the vertical *M*-gradient is zero:

$$\left.\frac{dM}{dz}\right|_{z=z_d} = 0 \tag{14}$$

The evaporation duct height essentially sets the top of the wave guide mechanism and is directly associated with the radar frequency that results in trapping of the EM waves (Kerr, 1951; Hitney and Hitney, 1990; Hitney and Veith, 1990; Rotheram, 1974). Surface-based ducts can result in similar effects on propagation, where the *M*-deficit (the difference between the maximum and minimum *M*-value in the inversion layer) is the

parameter that is most frequently examined (Sirkova and Mikhalev, 2003). Both the *M*-deficit and evaporation duct height have been shown to significantly impact propagation loss. The impacts of properties of surface-based ducts have been shown to extend to high elevations, particularly in the case of over-the-horizon radars (Hitney et al., 1978). Experimental measurements in evaporation ducts differ from theoretical and numerical simulation results primarily due to the lack of or minimal consideration of effects of the rough sea surface and atmospheric turbulence (Rotheram, 1974); the interaction of evaporation ducting phenomena with the sea surface greatly increases the complexity of the problem.

Though evaporation ducting is the most common, elevated ducting layers exist and have also been studied. Many numerical studies have examined the impact of combined surface and elevated ducts on propagation, particularly for over-the-horizon radars using a variety of modeling approaches including ray theory, mode theory, full wave solutions, and "waveguide formalisms" (Dougherty and Hart, 1979; Dresp and Ratner, 1977; Pappert and Goodhart, 1977). Furthermore, enhanced propagation observations over a 48.5 km trans-horizon path have been confirmed as being due to evaporation ducting and additional higher altitude ducts/super-refractive structures with PE modeling using Paulus-Jeske evaporation duct refractivity profiles (Gunashekar et al., 2007; Paulus, 1985). Full wave solutions are generally the most accurate when compared with observations (Dougherty and Hart, 1979), but discrepancies still occur. In these types of studies the refractivity is usually modeled as a bi/tri/multi-linear refractivity profile that is homogenous in range. Discrepancies are generally attributed to layer fluctuations and the existence of additional ducts that are not accounted for in the linear refractivity models

(Pappert and Goodhart, 1977). Wait and Spies (1969) demonstrate that even relatively weak surface and elevated ducts ($\Delta N = 4$ or 5 N-units) can modify the attenuation for centimeter wavelength radar waves, while Chang (1971) finds $\Delta N \geq 40$ N-units is needed at low grazing angles for VHF radar waves (meter wavelength). The effects of elevated ducts have also been shown to be polarization dependent (Chang, 1971).

Most of the studies mentioned thus far have been focused on the refractive structure of the atmosphere, particularly with regard to ducting and propagation effects. There are also numerous studies that examine the meteorological effects on refraction and propagation via experiments as well as numerical weather prediction (NWP). Most of these studies focus on the physical phenomena that result in the development of various refractive layers in the atmosphere. Bean and Dutton (1968) discovered the foundational relation that describes the dependence of radio refractivity on pressure, temperature, and water vapor pressure. Their work has paved the way for more recent studies, such as by Burk and Thompson (1997), who used a mesoscale NWP model that accounts for turbulence, radiative flux, and cloud physics to predict refractive conditions (e.g. ducting layers) in the MABL off the Southern California Bight. The mesoscale forecasts were correlated with *PF* measurements over two 130 km overwater paths at 375 MHz from the Variability of Coastal Atmospheric Refractivity (VOCAR) experiment. In particular, strong correlation was found between the ducting layer base height and *PF*. Various clear weather meteorological phenomena play a role in the refractive structure of the atmosphere, such as heat, moisture, and momentum transfer processes at the air-sea and inter air mass boundaries, elevated layer formation from subsidence, capping layers of the convective boundary layer, and weather fronts (Gossard, 1981; Reddy and Reddy, 2007).

Humidity fluctuations result in phase variation and angular displacement of radio signals and are due to dispersal of the nocturnal inversion, mixing through the capping inversion, convective structure in the capping layer and sub-cloud layer, as well as cold fronts (Coulman, 1991). Meteorological phenomena can also generate multipath effects even though multipath is generally associated with sea surface interactions. For example, Reddy and Reddy (2007) investigated deep fading (20-30 dB) caused by multipath from sea breeze circulation. The sea breeze circulation is found to cause a low-level super-refractive layer, accompanied by the formation of an elevated layer of high refractivity variance at the boundary of the cool humid and warm dry air. Reddy and Reddy (2007) conclude that specular reflection and scattering of radio waves from layered structures, along with multiple refractive paths, cause fast daytime fading.

As discussed in the prior section, the role of the sea surface introduces effects such as multipath. However, the sea surface can also change the impact of refractive ducting conditions on propagation. The rough sea surface is a complex and expansive topic, thus there are many studies that examine select aspects of the sea surface (Skolnik, 1990; Craig and Levy, 1991). In particular, there are three main aspects of the sea surface that have been examined: 1) how it changes some of the observed ducting phenomena previously discussed, 2) multipath effects and how they vary with roughness, and 3) how dielectric properties of the sea surface impact propagation. Of course, in the natural environment, all these factors occur and interact simultaneously. With respect to (1), most studies find that a rough ocean surface generally weakens the trapping effect of near-surface ducts (Hitney et al., 1985; Sirkova, 2012). Relative to (2), multipath occurs in the presence of any surface and roughening of the surface is generally found to

washout the interference pattern (i.e., reduce fade depth) but the extent of it is frequency dependent (Goldstein, 1951; Benhmammouch et al., 2009; Karasawa et al., 1990). And for (3), the dependence of the dielectric constant on the state of the sea surface impacts propagation loss through absorption and reflection mechanisms. The dielectric constant is frequency dependent (Johnson et al., 1998) and therefore introduces frequency dependent behavior of multipath (Skolnik, 1990) as well as modifications to it due to contrast of the dielectric constant between air and sea water (Bowditch, 2002). The reflection coefficient of seawater also varies with polarization, further complicating these phenomena (Kerr, 1951).

All the aforementioned studies focus on how specific aspects of the marine atmospheric environment affect radio wave propagation. Since these factors interact with each other, it is difficult to isolate the impact of specific phenomena, particularly for experimental studies where the environment is uncontrolled. For this reason, a few dedicated sensitivity studies have been undertaken to elucidate the specific effects of select parameters.

Haack et al. (2010) perform a validation and sensitivity study in the context of NWP. Four mesoscale forecasting systems were evaluated for the purpose of improving the ability to model boundary layer refractivity and atmospheric ducting in the marine atmospheric boundary layer (MABL). Four environmental models are used to predict refractivity profiles and duct characteristics. The statistics used to evaluate model validation are means, biases (defined as observation minus model), and root-mean-square-error (RMSE). These statistics also served as the basis for sensitivity testing. In validation, the four models are generally found to over-predict the mean moisture above

the surface layer, causing a weaker vertical gradient in specific humidity and yielding fewer and weaker ducts than observed in the MABL. Instrumented fixed-buoy time series were taken near the surface to measure sea surface temperature (*SST*), air temperature, relative humidity, wind speed, wind direction, and pressure, and helicopters were employed to take measurements of temperature, relative humidity, and pressure at higher elevations. These measurements were used to compute potential temperature, specific humidity, and modified refractivity. Sensitivity tests were conducted to determine the effect of the definition of the marine-atmosphere boundary condition (e.g., *SST* field and surface stability), NWP model initialization time, wind speed and direction, air temperature, pressure, and humidity on refractivity, ducting occurrence, and ducting strength. They found that improving the accuracy and resolution of the *SST* field component of the boundary condition, thereby reducing input uncertainty, had the most influence on prediction accuracy of coastal refractivity. An advanced *SST* analysis from the Navy Coupled Ocean Data Assimilation (NCODA) was used to produce the improved *SST* fields. Secondly, lengthening the NWP model initialization time was found to improve congruency to field calculations of potential temperature, specific humidity, and modified refractivity. Lastly, improving the quality of both the modeled *SST* fields and model initialization improved predictions of duct occurrence and strength. Interestingly, the overall effect of applying the NCODA *SST* analysis to one of the models was to reduce the specific humidity RMSE by half, although it also increased RMSE of potential temperature, especially near the surface. Withstanding the increased RMSE of potential temperature, the modified refractivity RMSE was reduced by approximately half because modified refractivity has a stronger dependence on humidity. This improvement enabled

better duct simulation, because these results yielded a stronger inversion layer, which supports more ducts. However, a higher false-alarm rate also occurred. Even so, the discrimination score rose, indicating the model has a better overall ability to accurately detect and characterize ducts (Haack et al., 2010).

Gerstoft et al. (2003) also specifically evaluated the sensitivity of clutter return intensity to refractivity parameters. A non-physically based parametric (i.e., mathematical) refractivity model was used. The refractivity model can account for ducting or non-ducting conditions. For range-independent analysis, changes in the base height, thickness, and mixed layer slope all shifted the location of sea clutter intensification. A relationship between these three parameters was seen and hypothesized to be linear. If a surface duct was present, the *M*-deficit parameter had a small effect on clutter return. In evaluating the sensitivity to range dependency of the refractivity profile, the clutter response was found to be state dependent. When the base height was varied about a starting value of 100 m, minor corruption to clutter intensification occurred between the range of 45 and 60 km. However, varying the base height about 40 m resulted in clutter return intensification features beyond 30 km being highly distinguishable from the horizontally homogenous case (Gerstoft et al., 2003), which suggests that lower altitude changes in base height may be more significant than higher altitude changes. Random *M*-deficit variations were not as influential as base height, which was found to be the dominant parameter in their sensitivity study.

A formal atmospheric sensitivity and validation study of the VTRPE simulation was performed by Doggett (1997). The study measured the sensitivity of the simulation to the accuracy and resolution of input atmospheric parameters for a 3 GHz signal (S-band).

Error profiles were created by varying the temperature, pressure, and relative humidity about values that represent defined refractive conditions (i.e., standard atmosphere), both individually and simultaneously. For example, the atmospheric parameter values used to create a standard atmosphere were deemed the physically accurate values for that given case; *T, P,* and *RH* were then varied to create different levels of error. Five levels of error were simulated in this manner for standard atmosphere, sub-refractive, elevated duct, and evaporation duct conditions. The main statistic used to measure the effect of the error on path loss was RMSE. Errors in humidity resulted in the greatest average RMSE in calculating path loss in standard and sub-refractive conditions. The overall average RMSE values ranged from 0.5% to 5%, and the maximum instantaneous path loss error was 20%. Validation results also showed that height readings by WSR-88D radar may have errors of over 3 km in a ducting environment due to the standard atmosphere assumption. The validity of assuming a homogeneous atmosphere was also tested using multiple soundings in the VTRPE simulation. In this case study, propagation path loss errors of up to 30% occurred as a result of assuming a homogenous atmosphere. The focus of the study was on the effect of individual atmospheric parameters, with limited cases of interactions examined. Sometimes, simulated errors had a cancelling effect on each other. For example, temperature error tended to oppose errors in humidity and pressure. The errors in propagation loss caused by individual parameters were found to be dependent on environmental classification (i.e., standard, sub-refractive, or ducting), in contrast to classification independent propagation loss errors that occurred when errors of all parameters (temperature, pressure, and humidity) were simulated. This result suggests that parameter interactions have an impact on path loss.

The sensitivity of path loss to meteorological data resolution was also tested using Penn State's MM5 mesoscale model refractivity profile output for the VOCAR experiment conducted off the Southern California coast in 1993 (Paulus, 1994). The horizontal and vertical resolution of meteorological and corresponding refractivity data generally had a small impact on path loss, though the vertical resolution had more effect, particularly for finer scale resolution changes. Vertical resolutions of approximately 50, 100, and 150 m from radiosonde measurements were used; it was found that decreasing the resolution from 50 to 100 m caused the most change in path loss. The weak dependence of path loss on resolution could have been due to the low variability of the *M*-profiles generated by the MM5 model and the difference in terrain resolution used by the MM5 model versus the VTRPE simulation. Limitations of the study by Doggett (1997) are that only a few parameters (pressure, temperature, and humidity) were examined at only one frequency (3 GHz) and sensitivity was evaluated using only a partial statistical analysis. Doggett (1997) recommended "a more thorough multivariate statistical study of the complex interactions of these parameters."

2.4.1 Extension of Prior Research

The current sensitivity study extends the research of Doggett (1997) through the use of a more advanced sensitivity analysis approach that captures interactive affects, including sea surface roughness effects, and examining multiple frequencies (3, 9, and 15 GHz) and polarizations (HH and VV). In contrast to Doggett (1997), the atmospheric parameters used in the current study are not meteorological, but rather mathematical, whose purpose is to characterize a wide variety of multi-layer refractivity profiles (see Methods section *3.2.1*). Doggett (1997) also suggests that using a high vertical resolution refractivity

profile model may be more important than using multiple range-dependent profiles because of the importance of the fine variations in refractivity at low altitude, especially near the transmitter. The regional variation of environmental parameter sensitivity is accounted for in the current study and we use a vertical resolution of 1 m, compared with the highest resolution of 50 m studied by Doggett (1997). The vertical resolution of 1 m is made possible by modeling, whereas the resolutions used by Doggett (1997) were limited by radiosonde capability. The current study quantifies interaction effects between all parameters using an advanced sensitivity analysis method (EFAST), providing insight into the combined effect of the atmosphere and ocean surface on propagation loss.

Similar to Doggett (1997), other sensitivity studies as well as general studies on various environmental effects on propagation tend to focus on only a few parameters at a time. In particular, the sensitivity studies mostly use the one-at-a-time method, where only one parameter is varied at a time. As outlined in the introduction and background, environmental effects interact with each other and can either cancel or compound effects of individual parameters. This study seeks to expand the current knowledge by performing a dedicated sensitivity study inclusive of both refractivity and sea state parameters using a sensitivity method (EFAST) that can account for parameter interactions. The objective is to better understand these competing and complimentary effects of the environment on propagation. Use of a global sensitivity approach, EFAST (Saltelli et al., 1999), can account for the interactive nature of these phenomena, and the propagation is modeled using the PE method (VTRPE), which is generally considered the most accurate for representing the effects of the environment on propagation (Sirkova, 2012).

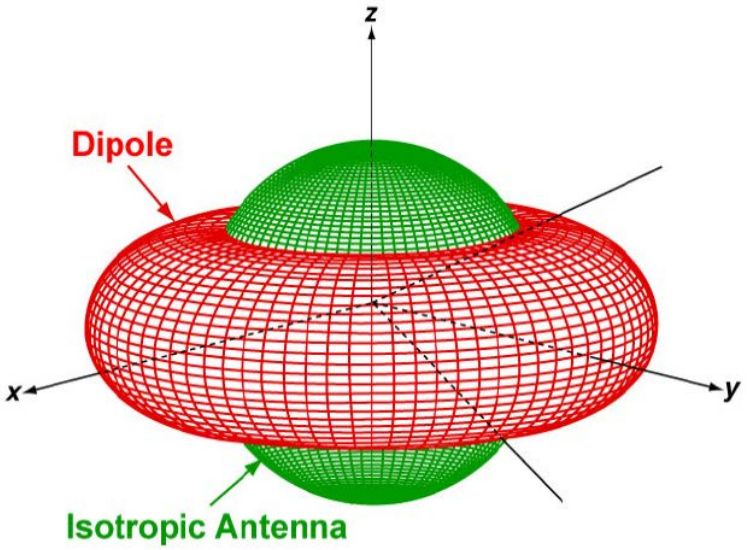

Figure 1: Dipole (red) and isotropic (green) antenna patterns from a source located at the origin (reproduced here from O'Donnell, 2007).

Figure 2: Parabolic radiation pattern produced by a dish antenna (reproduced here from Wolff, 2009).

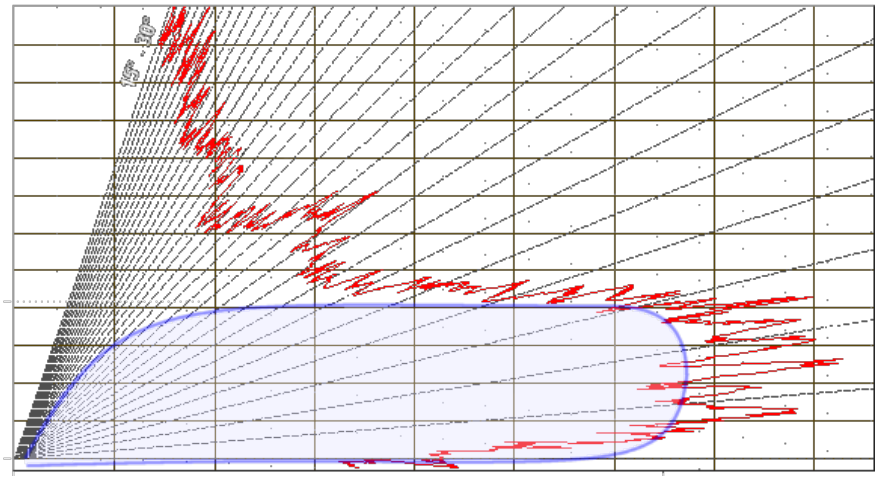

Figure 3: Cosecant squared radiation pattern with the radiation source at the origin. The vertical axis is height and the horizontal axis is range. The blue outline is the ideal depiction and the red outline is what can be expected in practice (reproduced here from Wolff, 2009).

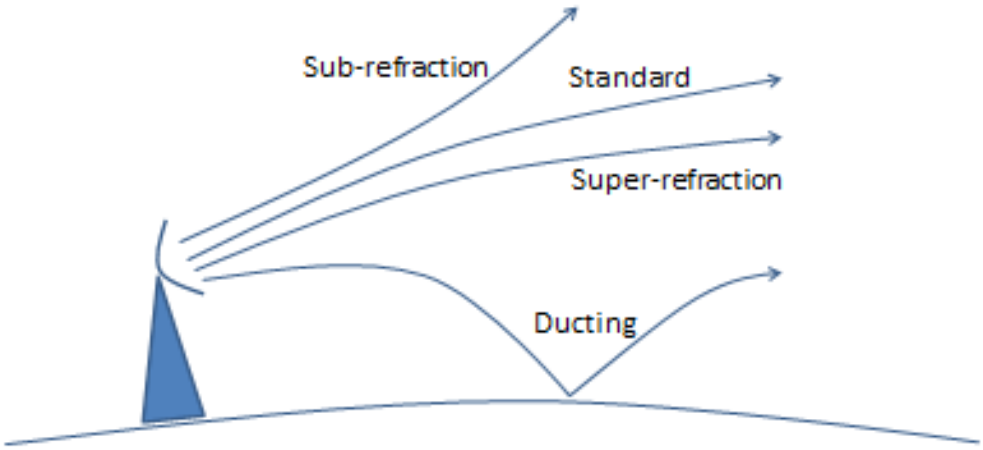

Figure 4: Classification of refractivity in the troposphere on radio waves.

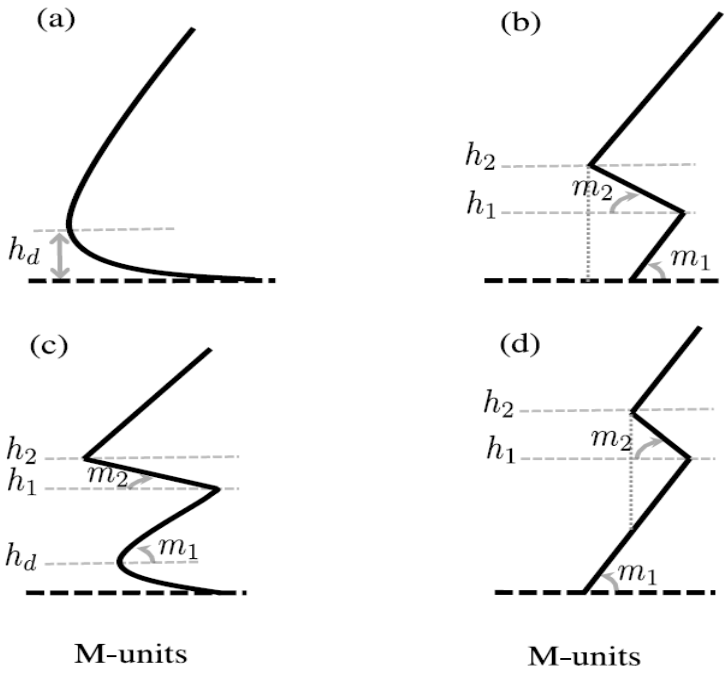

Figure 5: Diagram showing refractivity profiles of all types of ducts, with refractivity in *M*-units as the horizontal axis and height as the vertical axis: (a) Evaporation duct, where h_d is the duct height; (b) Surface duct, where duct height is defined from the surface up to h_2; (c) Combination of surface duct with an evaporation layer, with duct heights of h_2 and h_d respectively; (d) Elevated duct, where duct height is defined by the distance between h_2 to the intersection with the *M*-profile, shown by the grey vertical dotted line (reproduced here from Karimian et al., 2011).

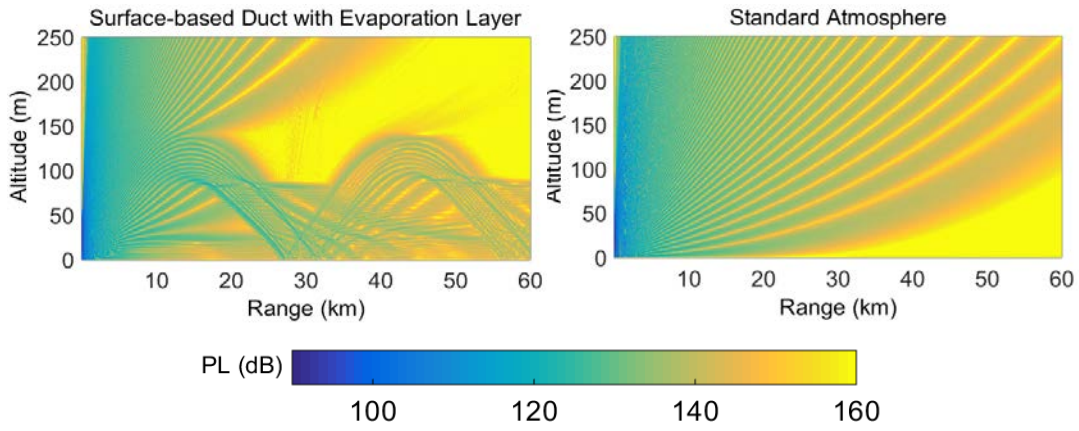

Figure 6: Simulated propagation loss for a surface-based duct with evaporation layer (left), with evaporation duct height of 36 m and surface duct (top of inversion layer) at about 140 m, compared with *PL* for a standard atmosphere (right).

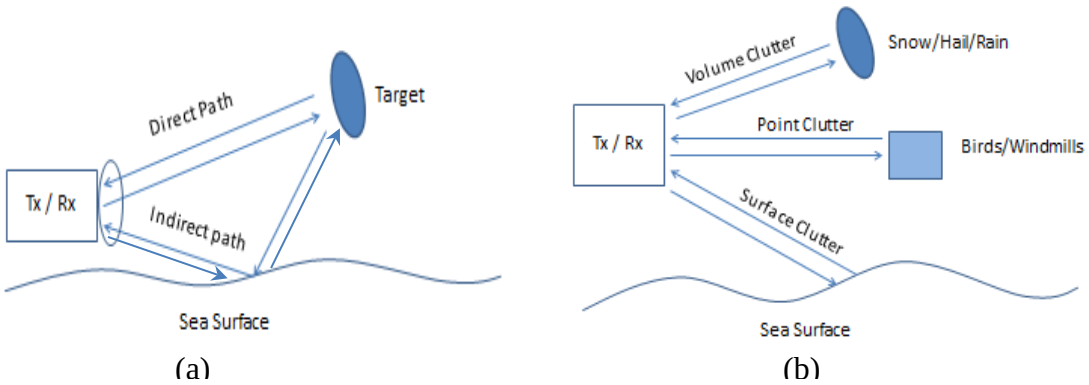

Figure 7: (a) Diagram showing multipath phenomenon; the direct and indirect signal paths are shown; (b) various types of clutter.

3.0 Methods

As discussed in the background (section *2.3.2*), the sensitivity analysis method best suited for this study is the EFAST method due to the complexity of the radar wave propagation simulation and the interactive nature of the modeled phenomena. In this section, the detailed implementation of the EFAST method for this study is explained.

3.1 EFAST

The EFAST method assigns a frequency, ω_i, to each parameter, X_i, using a transformation function:

$$X_i(s) = G(\sin \omega_i s) = \frac{1}{2} + \frac{1}{\pi}\arcsin(\sin \omega_i s + \varphi_i)\,; \quad -\pi \le s \le \pi\,, \tag{15}$$

where φ_i is a random phase shift that yields a more flexible sampling scheme (Saltelli et al., 1999). Eqn. (15) results in a uniform parameter distribution and a sample is shown in Figure 8 for sea surface temperature (*SST*).

The amplitudes of the oscillations of the output, *Y*, at frequencies ω_i and its harmonics reveal how sensitive *Y* is to parameter *i*. Following Saltelli et al. (1999), the simulation outputs, *Y(s)* (after removing the mean), are used to obtain the Fourier coefficients *A* and *B*, for each harmonic, *j*, discretely calculated as:

$$A_j = \frac{1}{N}\left\{Y_{N_o} + \sum_{q=1}^{\frac{N-1}{2}}\left(Y_{N_o+q} + Y_{N_o-q}\right) cos\frac{2\pi jq}{N}\right\} \tag{16}$$

$$B_j = \frac{1}{N}\left\{\sum_{q=1}^{\frac{N-1}{2}}\left(Y_{N_{o+q}} - Y_{N_o-q}\right) sin\frac{2\pi jq}{N}\right\} \quad , \tag{17}$$

where, N is the number of samples of s and $N_o = \frac{N-1}{2} + 1$. The total variance, V, the partial variance, V_i, and the partial variance of the complementary set, V_{-i}, can now be calculated by the following formulae (Saltelli et al., 1999, 2000; Ekstrom, 2005):

$$V = \frac{1}{N}\sum_{q=1}^{N} Y_q^2 \tag{18}$$

$$V_i = 2\sum_{j=1}^{M}(A_{j\omega_i}^2 + B_{j\omega_i}^2) \tag{19}$$

$$V_{-i} = 2\sum_{j=1}^{M}(A_{j\omega_{-i}}^2 + B_{j\omega_{-i}}^2)\,, \tag{20}$$

where, M is the number of harmonics included in the analysis. These variances are used to calculate the sensitivity index, *SI*, and total sensitivity index, *TSI*:

$$SI = \frac{V_i}{V} \tag{21}$$

$$TSI = 1 - \frac{V_{-i}}{V}, \tag{22}$$

for each parameter i. *SI* is a measure of the main effect and *TSI* is a measure of the total effect, including interactions.

The selection of the frequencies (ω_i and ω_{-i}) and sample size (N) involves trade-offs between aliasing, interference, and simulation runtime, which must be optimized. Aliasing is avoided when the Nyquist frequency, ω_{Ny}, is greater than $M\omega_{max}$, the highest frequency that occurs in the set (i.e., the highest harmonic of the highest parameter frequency). The Nyquist frequency is defined as:

$$\omega_{Ny} = \frac{N}{2} \tag{23}$$

Thus, in order to avoid aliasing:

$$N \geq 2M\omega_{max} + 1 \tag{24}$$

In this study, we use M=4, which is a common practice (Saltelli et al., 1999) and ω_{max} = 8; thus, we use N = 65 to avoid aliasing. This setup results in 1105 model runs for all 17 parameters considered (i.e., the product of Nk, where k is the number of parameters).

Interference occurs when harmonics of two different parameters have the same frequency value, and can lead to overlap in contributions to the variance of the output. Interference is unavoidable with a high number of input parameters (Saltelli et al., 1999); however, it can be minimized by using a high ω_i and low values of ω_{-i}. The maximum value of $M\omega_{-i}$ is half of ω_i, although larger separations are recommended at the expense of an increased number of samples to avoid aliasing (Eqn. 24). The higher harmonics of ω_{-i} usually converge to zero after a few harmonics. In order to minimize the number of samples, frequencies in the ω_{-i} set can be assigned the same value (Saltelli et al., 1999). For this study, the complimentary frequency set is assigned to one (ω_{-i} = 1). Consequently, interference with the parameter of interest occurs at the 8th harmonic of the complimentary set, which is four harmonics above that used to compute the partial variances of the complimentary set. Because this study examines a large number of parameters, even at the 8th harmonic there could be some interference; consequently, in lieu of increasing the frequency of the parameter of interest to further minimize the interference which would have resulted in many more model runs, we choose to incorporate a dummy parameter to account for this interference (Marino et al., 2008).

The dummy parameter has no effect on the simulation and consequently should have zero partial variance if no interference were present. Non-zero values of the dummy parameter *SI* and *TSI* therefore characterize the influence of interference on the results. The dummy sensitivity value is subtracted from that of all other parameters, thereby offsetting the influence of interference on the individual parameter results. We verify that the dummy distributions are significantly different from parameters that have sensitivity values above the dummy with a one-way ANOVA ($p < 0.05$) test to further validate this approach. While using a low sample size ($\omega_{max} = 8$) leads to unwanted interference effects, implementing the dummy parameter greatly mitigates these effects, while also minimizing the number of simulation runs required for the sensitivity analysis.

3.2 VTRPE Simulation

The Variable Terrain Radio Parabolic Equation (VTRPE) simulation is a physics-based radio wave propagation simulation that accounts for a wide variety of environmental effects (Ryan, 1991). It computes the full-wave solution of electromagnetic fields (amplitude and phase) and signal intensity in complex, spatially varying environments. The model uses cylindrical coordinates, and calculates the transverse components of the EM field by solving the scalar wave equation using a split-step rotated Green's function parabolic wave equation (GFPWE) derived from Maxwell's equations. The split-step Fourier method is used to employ the GFPWE in the frequency domain, with built-in stability and error controls. The simulation output used in this study is path loss (*PL*), measured in decibels. The magnitude and directivity of the signal are accounted for in path loss calculations (Eqn. 5). Radar frequencies between VLF and W-band (10 kHz-300GHz) can be simulated. The environment is modeled as a waveguide with impedance

or Fresnel type electromagnetic boundary conditions at the Earth's surface. Therefore, the radio waves can be classified as Transverse Electric (TE) or Transverse Magnetic (TM) waves. TE waves are horizontally polarized (HH) and TM waves are vertically polarized (VV). Effects of refraction, diffraction, and ducting due to variation of the atmospheric index of refraction are included. Terrain variability in elevation, roughness, and surface dielectric properties is simulated by VTRPE, as well as scattering and diffraction from rough surfaces.

3.2.1 Ocean Surface and Atmosphere

VTRPE generates sea surface realizations based on an empirical modified Donelan-Pierson-Banner type spectral model for the wind generated sea, which has inputs of surface (10 m) wind speed, U_{10}, surface wind direction, θ_w, and wave age, Ω (Apel, 1994). This wind-perturbed ocean surface incorporates a low wavenumber gravity wave spectrum and a high wavenumber capillary wave spectrum. A narrow-banded Gaussian swell component of the ocean wave spectrum is added, which has inputs of swell height, H_s, swell period, T_s, and swell direction, θ_s. Variable boundary conditions are included in VTRPE for water surfaces, such as the salinity and temperature dependent dielectric constant.

Refractivity is input directly as a vertical profile in units of modified refractivity (M-units) and is assumed homogenous in range. This multi-layer *M*-profile is mathematically produced by a variation of the "stacked" model (Figure 9) proposed by Gerstoft et al. (2003):

$$M(z) = M_0 + \begin{cases} M_1 + c_0\left(z - z_d\, ln\frac{z+z_0}{z_0}\right) & z \le z_L \\ m_{ML}z & z_L \le z \le z_1 \\ m_{ML}z_1 - \Delta M\left(\frac{z-z_1}{h_{IL}}\right) & z_1 \le z \le z_2 \\ m_{ML}z_1 - \Delta M + m_U(z - z_2) & z_2 \le z \end{cases}, \quad (25)$$

where, M_0 is the refractivity at the sea surface, z_L is the height of the evaporation layer, defined as (Gerstoft et al., 2003):

$$z_L = \begin{cases} \left|\frac{z_d}{1-\frac{m_{ML}}{c_0}}\right|, \; 0 < \frac{1}{1-\frac{m_{ML}}{c_0}} < 2 \\ 2z_d \;\; , \; otherwise \end{cases}, \quad (26)$$

where, z_1 is the base height of the inversion layer, z_2 is the height to the top of the inversion layer, and M_1 ensures continuity of the profile between the layers (i.e., it is not a free parameter). M_0 is determined based on the *SST* and assumes that the relative humidity (*RH*) is 100% (water vapor saturation). In reality, *RH* may be closer to 97% because of the salt content of sea water; but, this simplifying approximation only changes M_0 by 1.4% or less over the *SST* range. The evaporation layer is parameterized by z_0, the aerodynamic roughness height, c_0, the potential refractivity gradient as defined by Paulus (1990), and z_d, the evaporation duct height. The mixed layer is parameterized by its *M*-gradient, m_{ML}, and height, $h_{ML}=z_1-z_L$. The inversion layer is parameterized by its strength, ΔM, and height, $h_{IL}=z_2-z_1$. Finally, the upper layer is parameterized by its *M*-gradient, m_U.

The layer heights are used rather than the height values themselves (i.e., z_L, z_1, *and* z_2) in order to ensure that the layers stay in the proper vertical order regardless of the EFAST parameter value selection. In addition, because of the random parameter value selection

of the EFAST method, the inversion layer can result in generation of a surface or elevated duct above an evaporation duct; and when certain parameters are zero, some layers (e.g. ducts) may not be present. This parametric refractivity model does not consider the relationship between physical parameters of the environment and the refractivity profile. Consequently, the results of this sensitivity study only consider what regions (i.e., vertical layer) are most significant and what aspects (e.g., gradient, layer thickness) of the refraction profile *PL* is most sensitive to without considering what physical mechanisms might invoke these changes in the *M*-profile.

3.3 Numerical Experiments

The studied, two-dimensional domain is 0-1000 m in altitude, and 0-60 km in range with a resolution of 1 m and 0.05 km, respectively. The antenna parameters are selected to represent a generic air-sea surveillance radar. The transmitter properties are: 25 m transmitter height, csc^2 beam pattern, 15° vertical beam width (omnidirectional in azimuth), and -20 dB peak side lobe level. The main lobe elevation angle is 0° (pointed horizontally) and the beam cutoff angle is 45° below horizontal, where the beam cutoff refers to where the radiation pattern dramatically decreases in the csc^2 pattern. All antenna parameters are fixed, except frequency and polarization, which are varied on a case-by-case basis. The study is performed for frequencies of 3, 9, and 15 GHz at HH and VV polarization, giving 6 cases total (each of which require 1105 runs, see section 3.1).

The sensitivity analysis is performed for the parameters shown in Table 1. The ranges of the parameters are selected to encompass a multitude of conditions. They cover sea states of 0-12 on the Beaufort scale, *SST* and *SSS* ranges that cover the entire globe over

all seasons, and ranges of the stacked model parameters are similar to those used in Gerstoft et al. (2003). Because EFAST randomly generates the parameter values and very large ranges of parameter values are used, the potential for unrealistic refractivity profiles exists. Less than 0.2% of refractivity values (N-units) are less than or equal to zero and occur in less than 0.5% of the modeled profiles.

VTRPE computes the *PL* for every point in the domain, which is 1000 points (1 km) in altitude and 1200 points (60 km) in range. EFAST sensitivity computations (section 3.1) are applied to *PL* averaged over non-overlapping areas of 10 m x 0.5 km, resulting in *SI* and *TSI* distributions over the entire domain. Note that *PL* values are converted to *F* values before the averaging is performed and then converted back to *PL* values, having units of dB (see Eqns. 4 and 5). An example distribution is shown in Figure 10, which is already adjusted for the interference effects based on the dummy parameter. Performing the sensitivity analysis for these 10 m x 0.5 km areas permits evaluation of sensitivity variation, which can be high, throughout the 1000 m x 60 km domain, as Figure 10 demonstrates.

Table 1: List, description, and range of all environmental parameters examined in this sensitivity study. Parameters 1-8 are for generation of the ocean surface and parameters 9-16 are used in the "stacked" model for generation of the *M*-profile.

	Name	Description	Units	Range
1	SSS	Sea surface salinity	PSU	30 to 38
2	SST	Sea surface temperature	°C	1 to 35
3	Θ_s	Swell direction	° (CW from North)	0 to 359.9
4	Θ_w	Surface wind direction	° (CW from North)	0 to 359.9
5	H_s	Swell height	meters (m)	0.1 to 17
6	T_s	Swell period	seconds (s)	5 to 18
7	U_{10}	Surface wind speed	meters / second (m/s)	0.1 to 35
8	Ω	Wave age	(none)	0.83-3
9	z_0	Aerodynamic roughness height	meters (m)	7.5×10^{-5} to 1.5
10	c_0	Potential refractivity gradient	M-units / m	0.05 to 1.5
11	z_d	Evaporation duct height	meters (m)	0 to 50
12	h_{ML}	Mixed layer height	meters (m)	0 to 400
13	m_{ML}	Mixed layer refractivity gradient	M-units / m	0 to 0.4
14	ΔM	Inversion layer strength	M-units	0 to 100
15	h_{IL}	Inversion layer height	meters (m)	0 to 100
16	m_u	Upper refractivity gradient	M-units / m	0 to 0.4

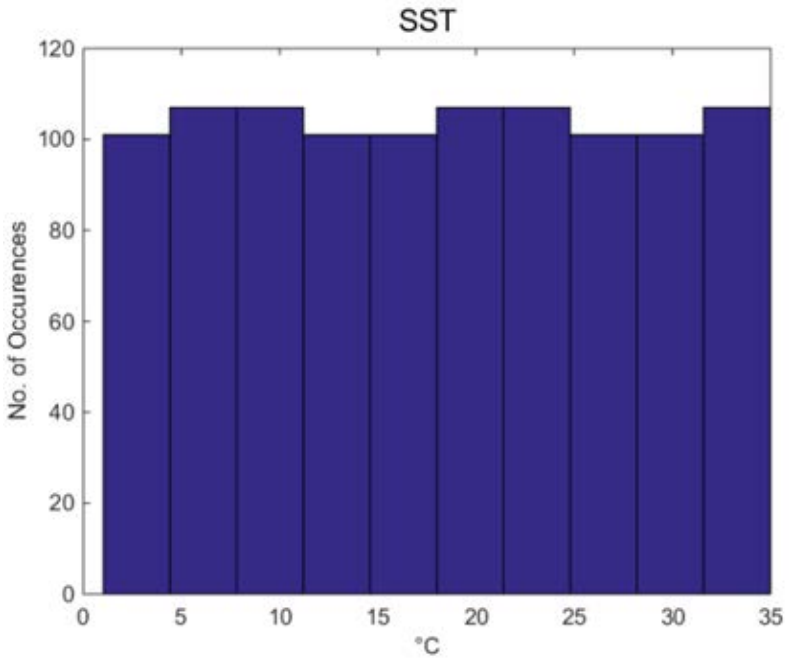

Figure 8: Example of uniform distribution for parameter *SST* (Eqn. 15).

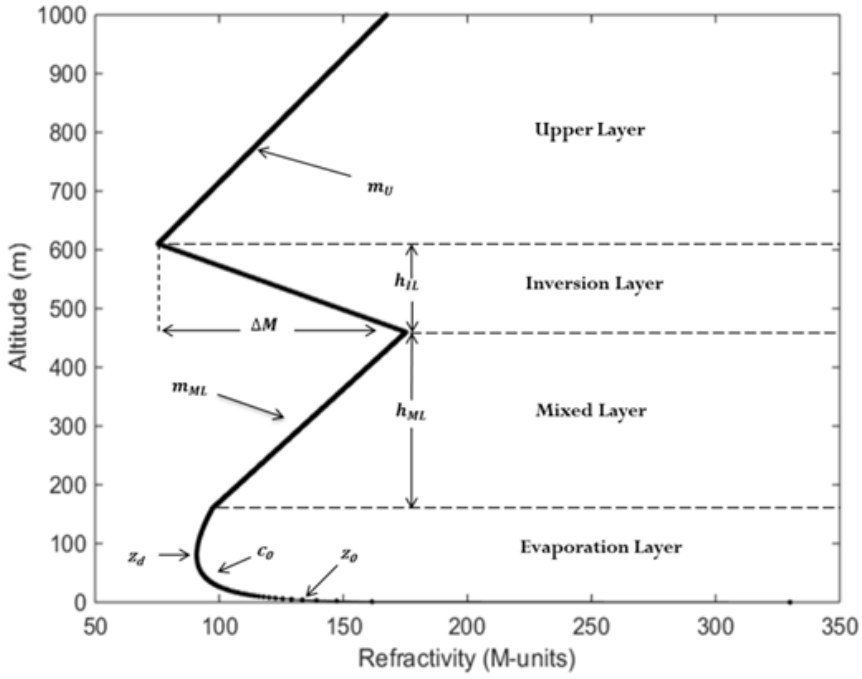

Figure 9: Sample *M*-profile produced by the "stacked" model, showing parameters for each layer (Eqn. 25).

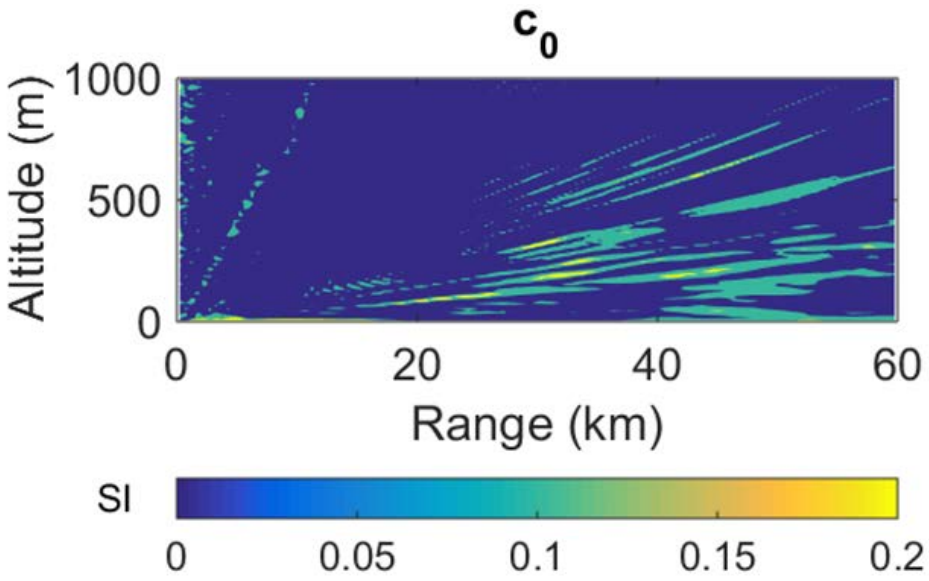

Figure 10: Example *SI* distribution for the potential refractivity gradient, c_0.

4.0 Results

To analyze the overall sensitivity of each parameter, the *SI* and *TSI* distributions are averaged over the whole domain (Figure 11). Sensitivity results change little with polarization as evident by comparing Figure 11a-c with Figure 11d-f. To further highlight this result, Figure 12 shows parameter rank versus *TSI*, where the VV case is the basis of the ranking order for all frequencies. Consequently, the VV curve always has a decreasing average *TSI* with rank and a difference in parameter rank for the corresponding HH case can be identified wherever the average *TSI* increases with rank. This indicator seldom appears in Figure 12 and only occurs at 15 GHz. As discussed in detail in subsequent sections, this discrepancy is likely due to an increase in the importance of ocean surface parameters at 15 GHz combined with the fact that radar wave energy reflected from the ocean surface varies with polarization (Fishback and Rubenstein, 1944). Frequency, on the other hand, has a significant effect on parameter sensitivity as evidenced in Figure 11 by the differences in parameter sensitivity distribution with frequency (across each row). In addition, there is generally a high degree of interaction between parameters, shown by the substantial difference between total effect (*TSI*) and main effect (*SI*), particularly for 3 GHz radar signals in the mid atmospheric layers (Figure 11). As expected, the atmosphere is generally more important than the ocean surface, indicating that atmospheric refractivity is more important than scattering and multipath effects from the ocean surface.

The importance of the atmosphere is most pronounced at 3 GHz and the *SI* and *TSI* values have a nearly normal distribution with elevation (for atmospheric parameters), with *SI* being proportional to *TSI* (Figure 11a; right side), the exception being the height of the inversion layer which has no significance. This result suggests a pattern of how sensitivity to the atmosphere changes with altitude, peaking at mid-level, where the mixed and inversion layers occur. At 9 and 15 GHz, the distribution is clearly not Gaussian with elevation, but the mixed layer height (thickness) is the most important both at leading and total order. In main order effect (*SI*), the mixed layer height becomes the leading parameter by a margin that increases with frequency and the other parameters are comparatively close to each other. However, these other parameters have *TSI* values that differ more from each other. The sensitivity distributions at higher frequencies imply that interaction effects of atmospheric parameters, while significant, are less distributed. Strikingly, the main effect of the mixed layer height is stronger than or nearly equivalent to the total effect of most of the other parameters at 9 and 15 GHz.

The ocean surface has an increasing overall effect on propagation with frequency, making it nearly as important as many of the atmospheric parameters at 9 and 15 GHz. The ocean roughness and dielectric parameters become increasingly important at higher frequencies, while the directionality of the ocean surface is most significant at 3 GHz.

To analyze how the sensitivity varies spatially throughout the domain, *SI* and *TSI* averages are taken over each of the regions shown in Figure 13. The range is divided at 10 km and 30 km, and the altitude is divided at 200 m and 600 m. Region sizes are primarily determined based on distance from the transmitter (i.e., smaller regions near the transmitter) because it is presumed that finer scale phenomena will impact *PL* closer to

the transmitter. In general, we do not want to average such trends out of the results by taking too large of an average near the transmitter. Regional results are presented in the sub-sections to follow.

4.1 Atmosphere

As previously discussed, the atmosphere has more effect on propagation loss than the ocean surface, which is a consequence of refraction and, in extreme cases, internal reflection effects from the atmosphere being more important than ocean surface scattering, multipath, and absorption. The distribution of atmospheric parameter sensitivity changes more significantly between 3 and 9 GHz than between 9 and 15 GHz (Figure 11), and suggests fewer parameters have a significant relative effect on propagation as frequency increases.

The mixed layer characteristics are the most influential over the entire domain, followed by the evaporation, inversion, and upper layers. The impacts of evaporation and inversion layers are well documented (e.g., Hitney and Hitney, 1990; Paulus, 1990; Wait and Spies, 1969), and this study confirms their importance. However, the importance of the mixed layer is not as well addressed. The high importance of the mixed layer height highlights the significant effect that vertical location and extent of each layer can have on propagation loss (Stephansen and Mogensen, 1979; Stephansen, 1981).

Past findings confirmed the importance of the vertical structure of the atmosphere by demonstrating that variations in this structure can cause significant variability in signal fades. For example, signal variations such as fade duration, number of fades, and signal level rate of change can be associated with fluctuations in layer structure (Stephansen and

Mogensen, 1979; Stephansen, 1981). Though the ocean surface is known to cause multipath propagation, reflection and refraction due to one or more layers in the atmosphere can also cause this phenomenon (Stephansen, 1981). Multipath fading caused by a single atmospheric layer has been modeled by Ruthroff (1971), where he shows three ray paths to be possible, depending on the height and thickness of the elevated layer. These types of effects are possible causes of the high sensitivity to mixed layer parameters because the mixed layer interfaces with both the evaporation and inversion layers. Furthermore, time variations in height, thickness, and refractivity gradient of atmospheric layers have been shown to account for rapid signal variations (Ruthroff, 1971). As illustrated in Figure 14, the mixed layer height and evaporation duct height are related to the inversion base height as defined by Gerstoft et al. (2003) for which they also find high local sensitivity. Thus, the key elements of the vertical structure of the atmospheric boundary layer are determined by h_{ML} and z_d. The importance of the mixed layer height at all frequencies reinforces the significant effect layer size and location has on propagation. A notable exception to the importance of the vertical extent of a layer in these results is the upper layer, for which location matters very little, indicated by h_{IL} sensitivity having no significance over the whole domain at all frequencies (Figure 11).

The character of these layers, represented by the mixed-layer *M*-gradient, duct curvature (dependent on c_0), aerodynamic roughness, and inversion strength (i.e., ΔM), is also important. The relative importance of vertical location versus character of the layers varies by region and frequency. The evaporation duct height, mixed layer refractivity gradient, and inversion strength are the most significant attributes of each respective layer

at 3 GHz; while at 15 GHz the evaporation duct curvature, mixed layer height, and inversion strength are most significant. The escalation in c_0 sensitivity at higher radar frequencies indicates an increasing sensitivity to the curvature of the *M*-profile, particularly in comparison to the significance of the evaporation duct height. Up to 9 GHz, the leading order effect of z_d is equal to or greater than c_0, but at 15 GHz c_0 overtakes z_d in leading and total order effect. But perhaps more importantly, when considering interactions, c_0 is more significant than z_d at 9 GHz. Moreover, the interaction effects (*TSI*-*SI*) of c_0 are significant and vary in proportion to changes in total order sensitivity, indicating that profile curvature must be known with reasonable accuracy at all frequencies to properly account for its total effect on propagation. Of course, the atmospheric parameters that most affect radar wave propagation depend to a degree on radar frequency and coverage desired, and sensitivity within different regions is discussed in the following sub-sections.

4.1.1 Evaporation Layer

The effect of duct height on propagation is the subject of numerous past studies (e.g., Hitney et al., 1978; Hitney et al., 1990; Karimian et al., 2013; Sirkova et al., 2003). The primary effect of the duct height is to roughly define the upper boundary of the waveguide mechanism, which can, for example, allow above average propagation power at long range. The results of the regional EFAST sensitivity analysis for evaporation layer parameters, shown in Figure 15, indicate the duct height to be the most influential parameter close to the transmitter (below 200 m and within 10 km), with and without considering parameter interactions. Note that in this and subsequent similar figures, the *SI* and/or *TSI* values are normalized by the maximum *SI* and/or *TSI* value for that region;

thus, a value of one indicates the most influential parameter in that region. Also, at altitudes well above the duct (> 600 m), propagation is sensitive at close range for both 9 and 3 GHz, but reduces with range only for 9 GHz. This frequency dependent behavior is most likely due to higher duct leak rates at lower frequencies, consistent with the findings of Hitney et al. (1978). Figure 15(a) also clearly shows that sensitivity falls off more rapidly with range as frequency increases, particularly at low altitude. These results are supported by Hitney et al. (1990), where they found effects of duct height to be dependent on radar frequency when examining frequencies in the same bands as this study. The maximum trappable wavelength is proportional to duct height (Kerr, 1951), meaning that lower frequency waves require greater duct heights to be trapped; therefore, duct height also determines whether or not trapping occurs, which partly explains some of the frequency dependent sensitivity, particularly at low altitude.

The other main parameter that defines the evaporation layer is, as defined by Paulus (1990), the potential refractivity gradient, c_0, which is a scaling parameter that affects the curvature of the evaporation duct *M*-profile. At higher frequencies and longer ranges, c_0 becomes more important than z_d, as shown in Figure 15. In general, less research has been dedicated to the study of duct curvature than duct height, particularly in short range applications such as the current study (<60 km). Refractivity inversion studies that have utilized the stacked model or Paulus-Jeske model generally use a fixed value for c_0 (-0.125 *M*-units/m) (Karimian, 2011). Recently, Karimian et al. (2013) have shown that the shape of the duct profile affects radar clutter and that the clutter power fall-off rates differ for 10 GHz versus 3 GHz. The results shown in Figure 15(b) also demonstrate that c_0 is influential at many locations within the domain. At low altitude, its importance is

approximately range-independent at the lower frequencies (3 and 9 GHz) and it becomes more important than the duct height at long range at the higher frequencies. At long range, propagation becomes more sensitive to duct shape as frequency and altitude increase. Interestingly, when comparing the two parameters over the whole domain, c_0 is more significant than z_d in all cases, except for 3 GHz (Figure 11). In general, as frequency increases to 9 and 15 GHz c_0 is more frequently (in-terms of number of regions) important than z_d, mostly due to interaction effects. Thus, because of the highly interactive nature of c_0, it may be considered a more important parameter at X and Ku band frequencies on average. In other words, at high frequencies, the shape of the evaporation duct is more important than its height in most regions of the domain.

4.1.2 Mixed Layer

Sensitivity analysis results, shown in Figure 11, demonstrate that the mixed layer has the strongest overall influence on radio wave propagation, likely due to its centralized location within the domain and large vertical extent. The mixed layer is parameterized by height, h_{ML}, and gradient of refractivity, m_{ML}. A notable exception to the dominance of the mixed layer is for 3 GHz, where the inversion layer strength, ΔM, is of about the same importance as h_{ML}in *TSI*, and at leading order (*SI*) the mixed layer parameters and evaporation duct height are most important. This result suggests that ΔM is a highly interactive parameter at this frequency, indicated by the large difference between *TSI* and *SI*. In the mixed layer at 3 GHz, m_{ML} has the strongest total effect (*TSI*). As frequency increases, h_{ML} dominates by a growing margin, suggesting that positioning of the mixed layer becomes increasingly important at higher frequencies. As shown in the regional results presented in Figure 16(a), at higher frequencies h_{ML} has the largest main order

effect over the majority of the domain. At long range, h_{ML} is the most sensitive parameter at all frequencies except when considering total order effects (*TSI*) at high altitude (Figure 16c). In this long range, high altitude region, ocean surface parameters, namely wind speed, aerodynamic roughness height, and swell direction and period have a strong total effect. These effects are discussed in the ocean surface section, but pointed out here to help explain the drop in h_{ML} *TSI* in this region.

The high importance of h_{ML} is likely due to its dominant role in determining the vertical location of the inversion layer, which in turn largely determines the height of anomalous propagation caused by elevated ducting mechanisms. These results are consistent with the findings by Gerstoft et al. (2003), where inversion layer base height is found to be the most influential refractivity profile parameter on propagation in their local sensitivity analysis. The only difference between the base height and mixed layer height is that base height includes the evaporation layer thickness if an evaporation duct is present (see Figure 14). In the absence of an evaporation duct, the mixed layer height equals the base height, as defined by Gerstoft et al. (2003). Because h_{ML} determines the height to the inversion (elevated duct) it is logical to associate h_{ML} with elevated ducting propagation. Radio waves are trapped when they are incident on the duct layer at angles less than a critical trapping angle (Dougherty and Hart, 1979). The maximum wavelength that can be trapped in a duct is proportional to the duct height (Kerr, 1951), and Wait and Spies (1969) find shorter centimetric wavelengths to be guided most effectively in an elevated inversion layer, i.e., lower attenuation rates. These findings imply that the probability of elevated ducting generally increases with frequency and decreases with grazing angle. Consequently, the high *SI* and *TSI* of h_{ML} (particularly at long range), shown in Figure

16, is consistent with the low grazing angle in this study, giving signals of all frequencies the greatest probability of becoming trapped in the duct. Following this logic, lower frequency signals would not be expected to get trapped as often at close range, thereby reducing propagation sensitivity to h_{ML}. This phenomenon is indeed demonstrated by the *SI* and *TSI* increasing significantly from mid-to-long range at 3 GHz as well as the increase in sensitivity to h_{ML} as frequency increases.

As with mixed layer height, the refractivity gradient is important because it affects neighboring atmospheric layers. It plays a role in determining the *M*-gradient transition with respect to the adjacent evaporation and inversion layers. A one-at-a-time (OAT) sensitivity test is performed to verify the effect of gradient transition between the mixed and inversion layers. The abruptness of the transition is quantified by the unit-less ratio of m_{ML} to m_{IL}, where

$$m_{IL} = \frac{\Delta M}{h_{IL}} \ . \tag{27}$$

Two cases are simulated in VTRPE, a gradual (m_{ML}/m_{IL}=0.18) and abrupt (m_{ML}/m_{IL}=1.29) transition, which are shown in Figure 17, at all frequencies. The transitions are modified by changing only the mixed layer slope and note that the changed mixed layer slope also impacts the transition between the evaporation layer and mixed layer, which is also more pronounced in the abrupt case. The average magnitude of the *PL* difference over all frequencies between these two cases is approximately 5 dB, with a standard deviation of about 2 dB, indicating a fair degree of variation throughout the domain, with *PL* differences exceeding 50 dB in some areas. The average *PL* difference increases slightly with frequency. It can be concluded from this OAT test that the mixed-layer transitions,

and presumably all atmospheric layer transitions, affect propagation loss. Because the height of the mixed layer is generally more significant than its gradient, it can be deduced that the location of anomalous propagation (above the mixed layer) plays more of a role than the propagation effects of the *M*-gradient magnitude and its change between layers (i.e., the transitions). It should also be noted that some of the abruptness of the transitions is an artifact of the stacked model in combination with the random parameter selection of the EFAST method. Consequently, the importance of the mixed layer slope could be slightly overestimated. In the natural environment, one might not expect such a sharp transition at the interface between layers, thereby reducing the importance of the mixed layer slope.

4.1.3 Inversion Layer

Elevated duct formation occurs when there is an elevated inversion layer, and can support propagation modes of exceedingly small attenuation (Wait and Spies, 1969). The inversion layer height is found to be of very little importance overall. However, the inversion layer strength is found to have moderate-to-strong significance, particularly when considering its interaction effects. This result is supported by Wait and Spies (1969), who found the most critical factors of an elevated tropospheric inversion to be refractive index contrast and effective radius of curvature, while the transition width (a measure of layer height) was found to be less important. Figure 18 shows the regional results for the inversion layer, where it is shown that at 3 GHz, ΔM has the highest total effect at two high altitude regions. Inversion layer strength nicely illustrates how much of an impact interaction effects have on propagation sensitivity, measured by the difference between *TSI* and *SI*, where interactive effects appear to be stronger at the

lowest of the three frequencies studied (3 GHz). As found by Gerstoft et al. (2003), leading order sensitivity to ΔM is relatively small for S-band radar. However, total order sensitivity is larger for all frequencies, especially for S-band, indicating that this parameter has significant interaction effects. As seen in Figure 18(d), the *TSI* of ΔM generally increases with range and altitude, except at high altitude long range. Additionally, at high altitude, ΔM sensitivity varies with frequency and range, and is the most significant parameter at low frequency in the mid and long range regions. The "hops" of a radar wave, defined as the downward reflection off an inversion layer (as in ducting), can affect propagation at ranges of 100-200 km or more (Kukushkin, 2004). In our study (60 km range), the 1st hop is the most likely to be observed, commonly acting at less than 100 km. This "hopping" behavior of radar waves between ducting layers offers a physical explanation of the increase in ΔM sensitivity with range. The maximally high sensitivity at high altitudes could also be due in part to upward leaking through the inversion layer as well, which is more significant at lower radar frequencies.

It is interesting to note that while the mixed layer height is the most important parameter overall, the inversion layer height is of negligible significance. The drastic difference in importance of the heights of these two layers, also found by Gerstoft et al. (2003), indicates that the vertical location of the inversion layer is much more important than its height. Consistent with expectations, our results show that the location and strength of an elevated duct are far more important than how high the duct extends, contrasting with the more important height of an evaporation duct. One physical explanation for this is that the transmitter is more likely to be inside an evaporation duct (for surface-based radar), creating a higher probability for trapping than in an elevated duct. By the time a signal

reaches the inversion layer, it has already been weakened and has a higher angle of incidence on the elevated duct, giving it a greater chance to propagate though it, which can lead to less diminished propagation and perhaps lower sensitivity. As previously mentioned, Wait and Spies (1969) show that shorter centimetric wavelengths are guided most effectively by an elevated inversion layer and Figure 18(b) supports these findings by showing that, at leading order, higher frequency waves are more sensitive to ΔM at high altitude. In contrast, there is a significant rise in the total effect of ΔM at low frequency (3 GHz; Figure 18d) due to interactive effects.

Because ΔM has a prominent effect on propagation largely due to interactivity with other parameters at 3 GHz, it is possible that it interacts strongly with parameters of neighboring layers, namely the M-gradients of the mixed and upper layers. ΔM essentially offsets the M-profile between the mixed and upper layers, and may affect the abruptness of the transition, which is known to effect propagation as demonstrated in the mixed layer section as well as discussed in the review paper of Stephansen (1981). In addition, an elevated inversion can reflect radar waves back into an evaporation layer, and lower frequency waves are more likely to cause secondary excitation of evaporation duct propagation in this manner (Kukushkin, 2004). This secondary excitation mechanism relies on conditions that allow for a nearly range independent refractivity profile (similar to the setup in this study), and implies the existence of potentially strong interactions between ΔM and the evaporation layer, which helps to explain the extraordinarily high *TSI* of ΔM at 3 GHz. Although the EFAST method cannot determine exactly which parameters ΔM interacts with strongly, the *TSI* of ΔM is followed more closely by c_0 than z_d, though both almost certainly interact with ΔM.

4.1.4 Upper Layer

The upper layer is characterized solely by its *M*-gradient, m_u. As seen in the regional results presented in Figure 19, m_u is most influential at high altitude presumably because the upper layer primarily occurs structurally in the high altitude regions; although, it is not the most important parameter at high altitude overall, indicated by the values being less than 1. In these high altitude regions, the total effect of m_u is strongest at lower frequencies (3 and 9 GHz), particularly at short-to-mid range. The total effect of m_u is generally more dispersed by frequency than the main effect, especially at high altitude, which indicates that interactive effects are frequency dependent. While the maximum range of this study (60 km) typically is not over the horizon, the maximum altitude (1000 m) is very similar to that examined by Hitney et al. (1978), who found an evaporation duct can influence beyond-the-horizon high altitude signals, and similar effects may be part of the interactions characterized in this study.

At mid-altitude and long range, m_u has moderate sensitivity, which is likely due in part to the upper layer commonly extending down into the mid-altitude regions. Interestingly, in this region, the main effect is more significant than the total effect, which means that interactions diminish the overall relative sensitivity of propagation power to m_u at all frequencies in this mid-altitude long range region. As expected, m_u is of little significance at low altitude.

Here, m_u is examined over the same range as its mixed layer counterpart, m_{ML} (0-0.4 *M*-units/m). Overall, the upper layer *M*-gradient is less important than that of the mixed layer for every frequency, even though the upper layer covers the largest area of the domain. This result further supports the prior conclusion that the relative position of a

layer has more effect on propagation than its size. While the upper layer *M*-gradient sensitivity may be due primarily to its role in the transition between the inversion and upper layers, a few other reasons could explain why it is less significant than the mixed layer gradient. First, the upper layer is farther away from the transmitter; therefore, radar waves may be more attenuated via scattering at this altitude and thus experience diminishing variability of *PL* relative to lower altitudes. Secondly, the upper layer is part of only one layer transition, whereas the mixed layer affects two transitions.

4.2 Ocean Surface

The ocean surface is complex and, accordingly, affects radar waves in a complicated manner. It is expected that forward propagation will depend on all parameters that describe the state of the sea surface, particularly given the known complexities of sea clutter (backscatter), which depend on wind speed and direction, frequency, grazing angle, and polarization, among other factors (Skolnik, 1990). The main mechanisms through which the ocean surface affects radar wave propagation are absorption, reflection, and scattering.

For this study, the ocean surface has been divided into 3 sub-sections: dielectric properties, directionality, and roughness. The overall effect of the ocean surface on radar wave propagation is frequency dependent, as seen in Figure 11, with a broader range of sensitivity to ocean surface parameters at higher frequencies. A good example of frequency dependence is seen in the dielectric parameters, which clearly become more important with frequency. At low frequency (3 GHz), the directionality parameters are the most important aspect of the sea surface. Directionality, in combination with swell

period, primarily affects the large-scale roughness of the sea surface, which according to these results, is more important at low radar frequencies.

The geometry of the rough ocean surface undoubtedly plays a strong role in how it affects radio wave scattering. The sensitivity to roughness of the ocean, shown in Figure 11 is primarily due to swell period, T_s, and aerodynamic roughness height, $z_{0,}$ where the latter only affects the refractivity profile in this study. Interestingly, the swell height has very little significance at any radar frequency. The importance of wind speed and consequently wind seas, however, increases with frequency, suggesting smaller scale roughness factors are more important at higher radar frequencies.

4.2.1 Dielectric Properties

The dielectric properties of sea water, sea surface salinity (*SSS*) and temperature (*SST*), influence reflectivity. Because the dielectric constant generally increases with decreasing frequency (Johnson et al., 1998), it is expected that the sensitivity of dielectric parameters would be frequency dependent as demonstrated in Figure 11. On average, the reflection coefficient of seawater is greater for radar waves of HH polarization than VV (Kerr, 1951). This difference appears to be underrepresented in the sensitivity results of *SSS* and *SST* as demonstrated by the similar normalized *TSI* between HH and VV polarization (c.f., Figure 20). Such underrepresentation may be due to our neglect of backscattering from the sea surface, a process that is dependent on polarization. Because salinity has a stronger influence on conductivity (which affects reflectivity and absorptivity), *SSS* generally has a stronger effect on propagation than *SST*. Haack et al. (2010) finds *SST* to be highly influential on the refractivity profile of coastal environments. Our study finds the effects of *SST* on radar wave propagation power to be minimal relative to the other

parameters, except in certain regions, where we use the *SST* as a dielectric property and to determine the surface refractivity value. As seen in Figure 20, there is more variation in total sensitivity of *SSS* with space and frequency than *SST*.

The sensitivity of *SSS* and *SST* generally increase with range at low altitude (Figure 20), and also at mid-altitude for *SSS*. At mid-range and mid-to-high altitude, there is a marked insensitivity to *SST*, which corresponds almost exactly to the region of near constant reflected wave field strength in an experimental study by Kerr (1951): 10-30 km in range and 152-1,524 m in altitude. The *SSS* sensitivity is higher than that of *SST* in these regions at mid-to-high frequencies, and is relatively constant with altitude at all frequencies, with the exception of VV polarization at 15 GHz experiencing a rather significant jump in *TSI* at high altitude. At long range, *SSS* and *SST* importance exhibit a simultaneous variation with frequency and altitude. That is, as altitude increases, higher frequency signals continue to be sensitive to *SSS* and *SST* while their sensitivities at lower frequencies diminish. However, at short range, this trend is reversed for *SSS*, where relative importance of lower frequency signals increases with altitude; but, in general, the sensitivity is much lower at short-range. For *SST*, low frequency signals are most sensitive at short range. At high altitude there is a correspondence between range and frequency for overall importance of *SSS* for HH polarization (i.e., low frequency is most important at short range, mid frequency is most important at mid-range, etc.). Interactive effects (*TSI-SI*) are small for *SST* in comparison to other parameters.

Because the dielectric properties of seawater affect reflection and scattering from the surface, salinity and temperature also affect propagation loss through the multipath mechanism. A phase change occurs when a radio wave is reflected from a surface with a

different dielectric constant, and the amount of this phase change varies with conductivity, which is related to the dielectric constant (Bowditch, 2002). Therefore, the variation in the dielectric constant caused by salinity and temperature changes at the surface results in phase variation of reflected radar waves, and thus interference patterns. This effect likely causes a spatial shift in the multipath pattern, and that shift would be more pronounced farther from the surface and transmitter, consistent with the increased sensitivity at high altitude and/or long range, particularly at high-frequency. The alternating fade pattern produced by multipath propagation is frequency dependent with more finely spaced multipath "striations" at high frequencies (Skolnik, 1990). This frequency dependence is partially due to the dielectric constant being dependent on frequency. Furthermore, Kerr (1951) illustrates that the effect of reflected radar waves on field strength varies with range due to changes in grazing angle and lobe structure, where regions of finer lobe structure are due to rapid variation of the phase difference of incident and reflected rays with position. Thus, multipath effects can help explain the significance of *SSS* at high frequency, short range, and low altitude (where multipath effects vary most rapidly with position). For longer ranges at low altitude, the lower frequency signals are more affected by *SSS* in comparison to short range, suggesting that shifts of the multipath lobe structure are more significant farther from the transmitter, consistent with the coarser multipath striations at lower frequencies.

4.2.2 Directionality

The wind and swell direction, θ_w and θ_s, are generally most important at 3 GHz, the longest radar wavelength studied, as seen in Figures 11 (whole domain) and 21

(regional). The total sensitivities at higher frequencies (9 and 15 GHz) are similar throughout the majority of the domain.

At low altitude, the sensitivity of swell direction decreases with range at a rate that is frequency dependent (Figure 21a). At this altitude, in the long range region, the sensitivity to directionality is nearly zero at all frequencies; however, in the short range region, the importance of θ_s and wind direction (i.e., wind seas), θ_w, is nearly equal at all frequencies. Both θ_s and θ_w exhibit a peak in frequency dependence at mid-range. Swell direction tends to become increasingly significant with altitude, particularly at mid-to-long range and low-to-mid frequency, while the wind direction tends to be most significant at low altitudes. In fact, swell direction is the most important parameter at long-range high-altitude at 3 GHz. These results suggest that sea directionality due to the local wind wave spectrum is more important closer to the sea surface and direction of the swell spectrum is more important at higher altitudes at mid-to-low frequencies. Consistent with these results, Karasawa et al. (1990) shows multipath fading to be slightly higher (1-2 dB) for swell dominated seas than wind-wave dominated seas.

Skolnik (1990) discusses the dependence of wind direction on sea clutter, which is strongest viewed upwind, weakest crosswind, and of intermediate strength downwind. Although this study ignores backscatter returns, its dependence on wind direction could provide insight into the effect of θ_w on forward propagation. In particular the relative difference between wind and swell direction (θ_w - θ_s) may be important because an opposing wind will raise the wave height and a wind aligned with swell flattens the wave (Wetzel, 1990). The large difference between *TSI* and *SI* for directionality parameters (Figure 11) indicates that they are highly interactive parameters when *TSI* is high (i.e., at

3 GHz). Using PE modeling, Benhmammouch et al. (2009) also verifies the effect of wind direction on propagation loss at X-band frequency (9 GHz). These authors show that path loss is lowest when the angle between EM wave propagation and wind direction is 90° (crosswind), and greatest at 0°. In general, Figure 21 shows sensitivity to θ_w and θ_s to be lower for high frequency signals, suggesting that other parameters play a more significant role in the variability of propagation loss at these frequencies.

4.2.3 Surface Roughness

Sea surface roughness is challenging to analyze, because it is influenced by all 8 ocean parameters. The five selected in this study as "roughness" parameters are chosen based on the hypothesis that they play the most dominant role in characterizing the roughness of the sea surface: swell height (H_s), swell period (T_s), wind speed (U_{10}), wave age (Ω), and aerodynamic roughness height (z_0). The aerodynamic roughness height is varied independently from wind speed and swell height, and only impacts the refractivity profile through the stacked model (Eqn. 25). Although unrealistic, this setup is an unavoidable consequence of the EFAST method, which requires that parameters be varied independently. The wind speed and wave age are used to generate the local wind-driven sea surface. The numerical study utilizing a PE propagation model performed by Benhmammouch et al. (2009) examines the effects of large and small scale sea surface roughness on X-band radar waves (9 GHz) in the presence of an evaporation duct, and finds sea surface roughness to significantly affect path loss. In our study, we find that roughness attributes that affect *PL* most are swell period and wind speed.

There is a high degree of interaction (*TSI-SI*) for roughness parameters over the whole domain with the swell period being the most interactive parameter at 9 and 15 GHz. For

total order sensitivity, T_s and z_0 are dominant roughness parameters for all frequencies (Figure 11), while wind speed also becomes important at mid-to-high frequencies. Regional results for roughness parameters are shown in Figure 22. In Figure 22c, at low altitude, swell period is significant at all ranges and frequencies. At high altitude, the importance of swell period increases simultaneously with range and frequency (i.e., at short range it is most important at low frequency, mid-range at mid-frequency, and long-range at high-frequency).

Swell height *TSI* varies with frequency and region (Figure 22b). However, it is generally not a significant factor at higher frequencies while it maintains some importance for 3 GHz signals, particularly at low altitude as well as at short-range high altitude. Using PE modeling, Craig and Levy (1991) show that a rough sea (2 m wave height) reduces the depth of close-in multipath nulls significantly, especially at short range, where the grazing angle is highest. These results are consistent with sensitivity to swell height being generally largest at short range, particularly at low frequency for *SI* (Figures 22b and 23d) despite the low grazing angle of this study. Furthermore, the large *SI* of H_s at short range for low frequency is likely influenced by the path loss lobes being thicker. Also noteworthy, H_s is of nearly zero importance along the diagonal path from the transmitter to the high altitude, long range region. Karasawa et al. (1990) shows multipath fading to be dependent on wave height, frequency, and grazing angle. At low grazing angles, the results of their study indicate that lower wave heights cause more multipath fading, with the maximum multipath fade depth occurring in a calm sea (0-0.5 m wave height) at very low grazing angles. Karasawa et al. (1990) also find that multipath fade depth varies little with wave height and frequency (ranging between 1-10

GHz) for swell dominated seas. In contrast, our results show that swell period is important, but we find consistent results regarding the swell height. As previously mentioned, swell period is a highly interactive parameter; thus, the discrepancy between this study and that of Karasawa et al. (1990) is likely because interactive effects were not considered in their study because we also find relatively low sensitivity to swell period at leading order (Figures 22c and 23c). Because swell period is related to wavelength of the swell, these sensitivity results imply that wavelength is more important than wave height. In other words, for ocean swell, propagation is more sensitive to the number of ocean wave peaks than their height. The relative importance of wavelength over wave height is somewhat more pronounced at higher frequencies.

Wind speed has zero effect on propagation on average over the whole domain for 3 GHz (Figure 11), but becomes much more important at 9 and 15 GHz. There is generally a relationship between sensitivity and altitude and frequency, where higher frequency signals show greater sensitivity at higher altitudes, particularly at mid and long range; however, the *TSI* of U_{10} decreases with altitude at low frequency (Figure 22e). The significance of U_{10} generally increases with range, where it is basically unimportant at short range. Slight differences between HH and VV polarizations are also found for this parameter. Surprisingly, U_{10} is the most important parameter at long range, high altitude at mid-to-high frequency. Karasawa et al. (1990) finds that "wave height dependence becomes more pronounced for higher frequencies" for wind seas, which is consistent with our results. They also found multipath fade depth to generally decrease with increasing frequency and wave height for wind seas, except at wave heights below about 2 m (Karasawa, 1990). Of all grazing angles, radar frequencies, and sea states studied,

the maximum fade depth occurs at the lowest grazing angle (1°) in calm seas. This multipath behavior is likely the case in the current study because of the low grazing angles.

Aerodynamic roughness height shows similar trends as U_{10} at mid-to-high altitudes, despite the fact that they are varied independently. Thus, changes in the local wind-wave spectrum due to U_{10} and z_0 are most important at high altitude long range, presumably because of their effect on multipath shifting in this region. Note that a large portion of their effect in this region is due to interactions, evident by the large discrepancy between *TSI* (Figures 22a and 22e) and *SI* (Figures 23a and 23b), particularly at the higher frequencies. At low altitude, importance (*TSI*) of aerodynamic roughness decreases with range while it increases with range for wind speed. This result implies that smaller-scale effects associated with z_0 and its impact on the evaporation duct *M*-profile occur at short ranges and more surface interaction is needed before the wind speed effects are significant, thereby occurring at longer ranges. The importance of z_0 at short range, low altitude is consistent with other evaporation layer parameters being important in this region (Figure 22a). Gerstoft et al. (2003) and Paulus (1990) find little dependence of the atmospheric evaporation layer refractivity profile on z_0, which is consistent with the leading order sensitivities being relatively low at all regions in the domain (Figure 23b); however, when interaction effects are considered, its importance increases, particularly at high altitudes (Figure 22a).

Wave age has zero significance over the whole domain on average at every frequency (Figure 11). It is mostly significant at low altitude for the 3 GHz signal (Figure 22d), and there is a significant difference in VV and HH sensitivity at short range high altitude.

Radar waves propagating through an evaporation duct over a rough sea surface experience competition between trapping and surface scattering (Hitney et al., 1985). This competition occurs because the attenuation rate of well-trapped modes is decreased by the duct and increased by roughness. Because higher frequency signals are more likely to be well-trapped, they are also more likely to contact the surface more frequently and attenuate more. At high enough frequencies (well above those in this study) the attenuation rate levels off. Sea surface roughness generally destroys the trapping property of the duct structure and changes the path loss (*PL*) pattern (Sirkova, 2012).

In addition, surface roughness affects the interference pattern of radar waves. This impact is most evident for higher frequency waves because the lobes are narrower and more numerous, which make them more susceptible to "washout" of the interference pattern (Goldstein, 1951). Also, shadowing increases the destructive effect of sea surface roughness on duct trapping ability, especially for long range propagation (Sirkova, 2012). Specular reflection is also greatly diminished by sea surface roughness and can cause significant signal strength variation over short ranges, while scattering effects of roughness on *PL* are more noticeable over longer transmission paths (Kerr, 1951). Because of all these competing and/or complimentary effects, interaction effects associated with sea surface roughness can be significant, consistent with our current findings (Figure 22 versus Figure 23). In general, the significance of ocean surface roughness on propagation seems to increase with frequency, especially at higher altitudes.

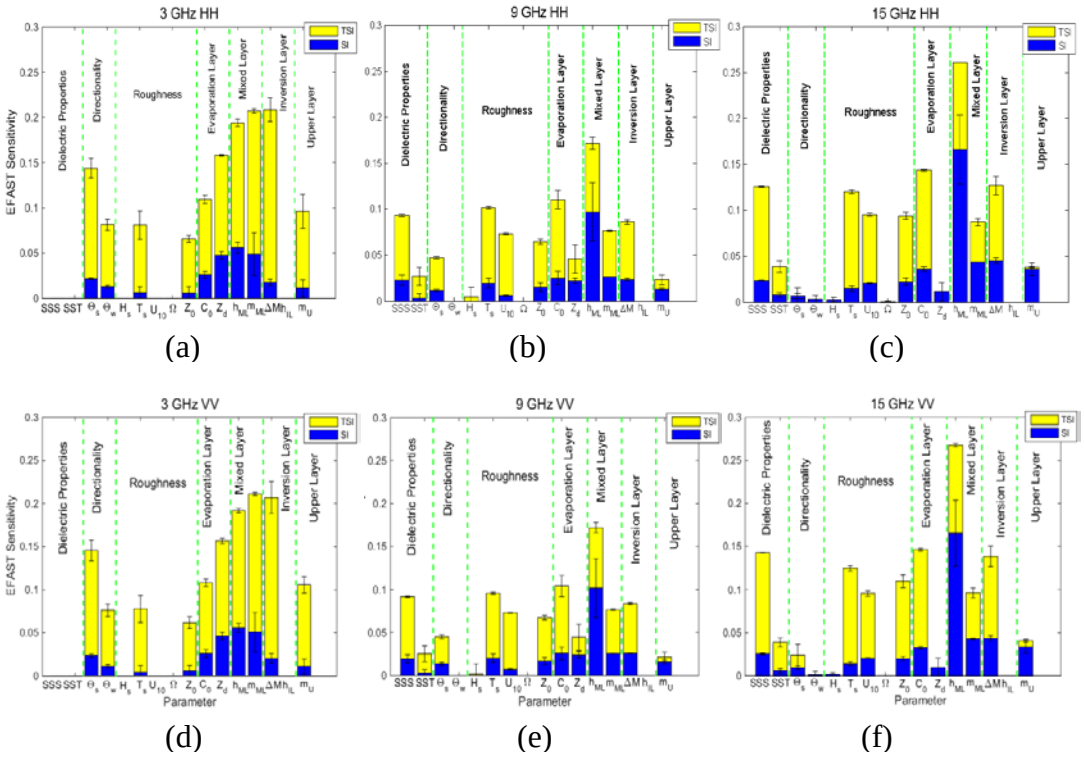

Figure 11: Main order (*SI*, blue) and total order (*TSI*, yellow) sensitivity results averaged over the whole domain for 3, 9, and 15 GHz as denoted in each subfigure title; (a-c) are for HH polarization and (d-f) are for VV polarization. The error bars indicate the variability of the *SI* and *TSI* values over the domain.

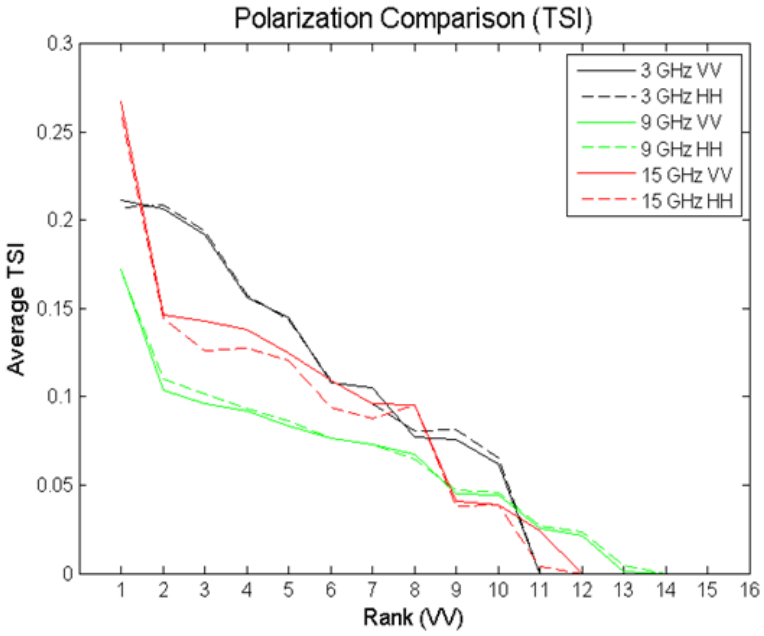

Figure 12: Plot of parameter rank versus average *TSI* for all frequencies and polarizations. For each frequency, the HH case is plotted using the ranked order of parameters for the VV case. The VV case will therefore always decrease with increasing rank. Points where the HH results do not decrease with increasing rank indicate a difference in rank between HH and VV parameters for a given frequency.

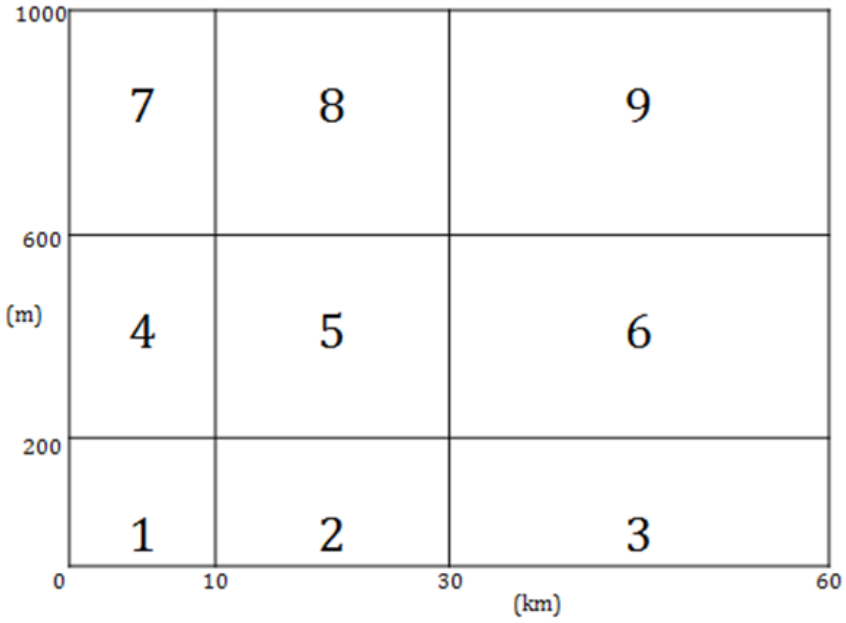

Figure 13: Definition of regions (1-9), referred to as low, mid, or high range/altitude.

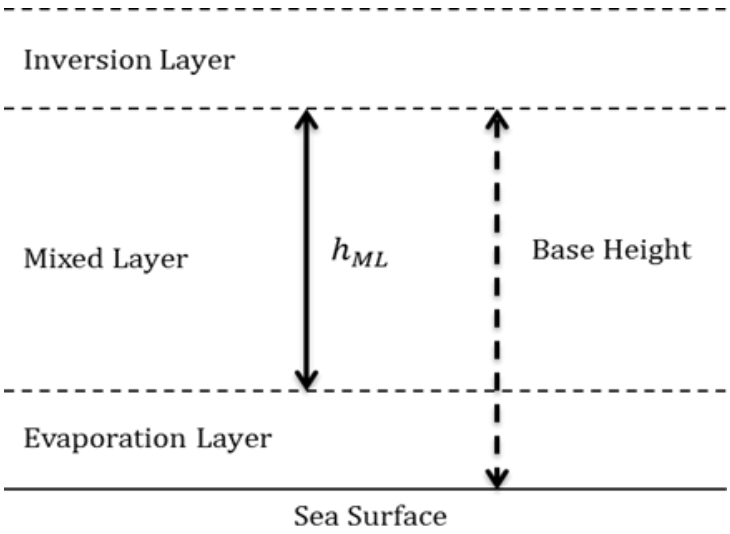

Figure 14: Illustration of the relationship between mixed layer height (solid arrow), inversion layer base height (dashed arrow), and the evaporation layer, which is defined based on the evaporation duct height (Eqn. 26).

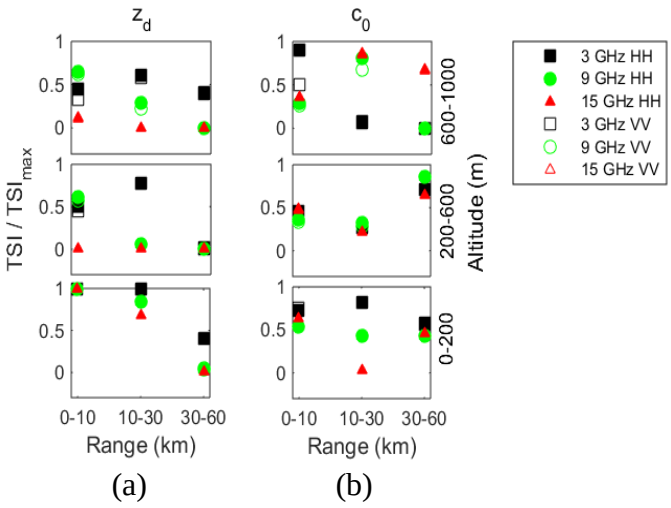

Figure 15: Normalized *TSI* by region of (a) z_d and (b) c_0 for 3, 9, and 15 GHz at HH and VV polarizations (see legend). Note a value of 1 on the vertical axis indicates the most influential parameter in that region.

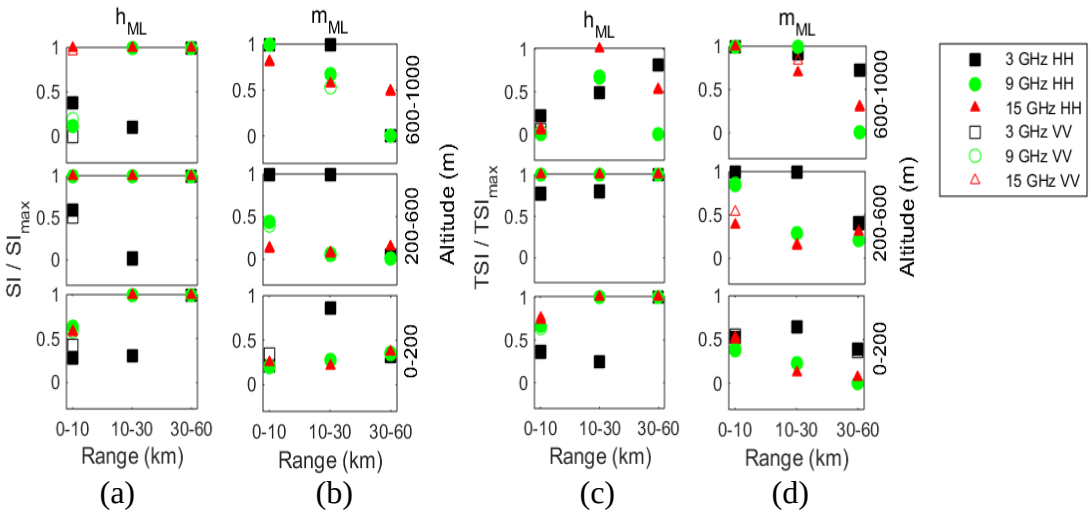

Figure 16: Normalized *SI* (a and b) and *TSI* (c and d) by region for mixed layer height and refractivity gradient.

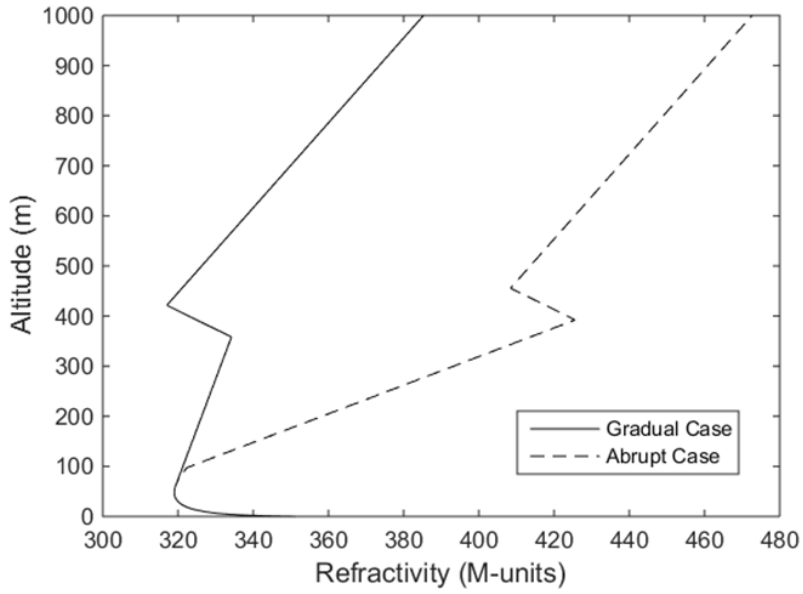

Figure 17: *M*-profiles for the "gradual" (m_{ML}/m_{IL}=0.18) and "abrupt" (m_{ML}/m_{IL}=1.29) transition cases.

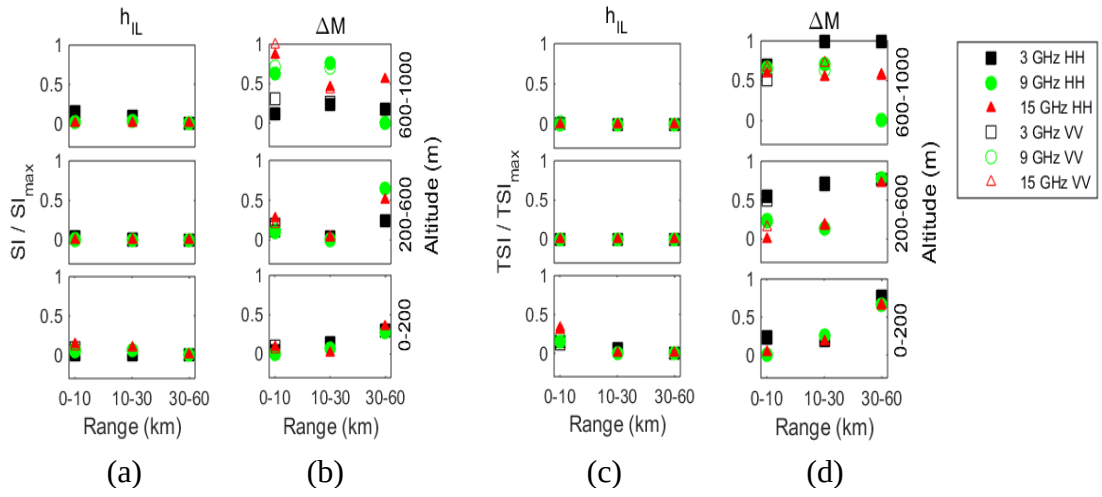

Figure 18: Normalized *SI* (a and b) and *TSI* (c and d) by region for inversion layer height and strength.

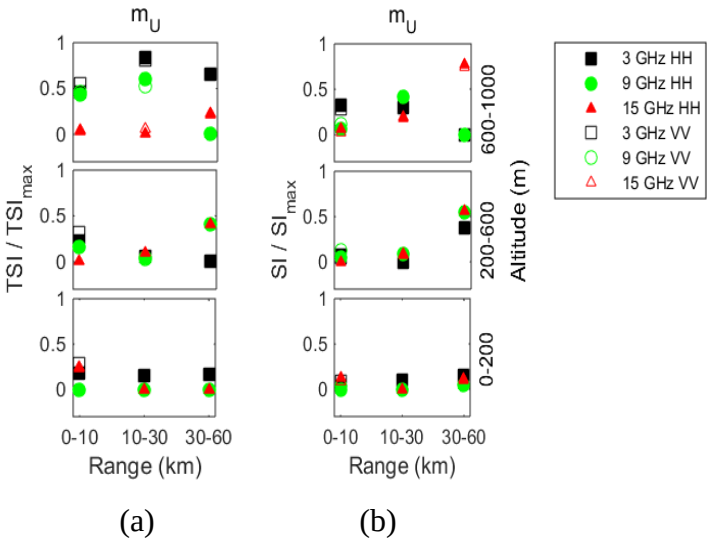

Figure 19: Normalized sensitivity by region of m_u for (a) *TSI* and (b) *SI*.

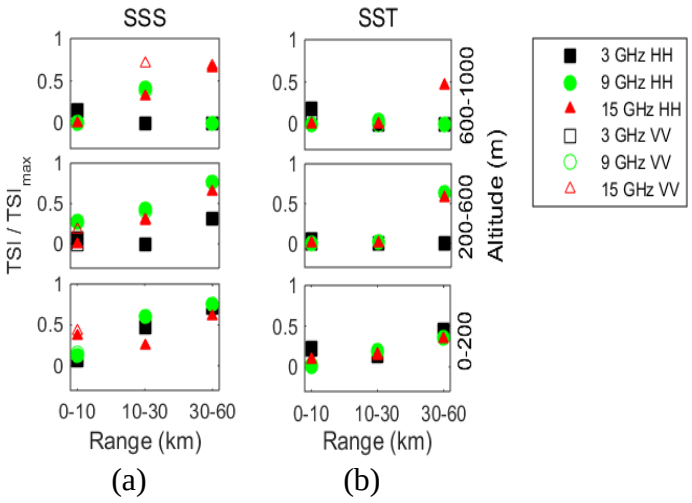

Figure 20: Normalized *TSI* by region for (a) salinity and (b) temperature, of the sea surface.

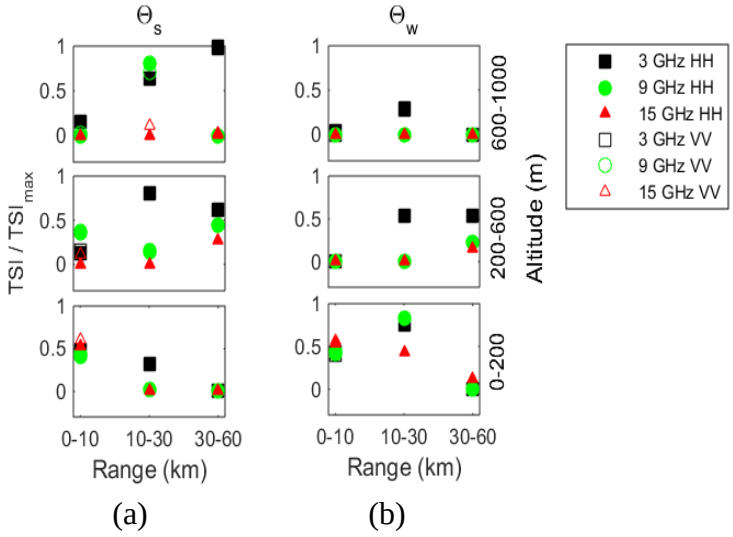

Figure 21: Normalized *TSI* by region for (a) swell direction and (b) wind direction.

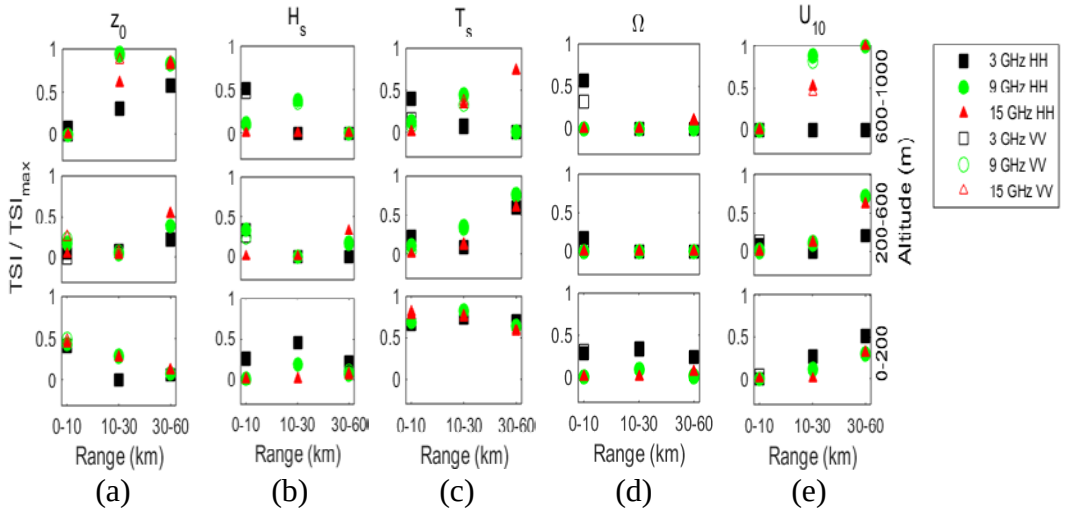

Figure 22: Normalized *TSI* by region for roughness parameters: (a) z_0, (b) H_s, (c) T_s, (d) Ω, and (e) U_{10}.

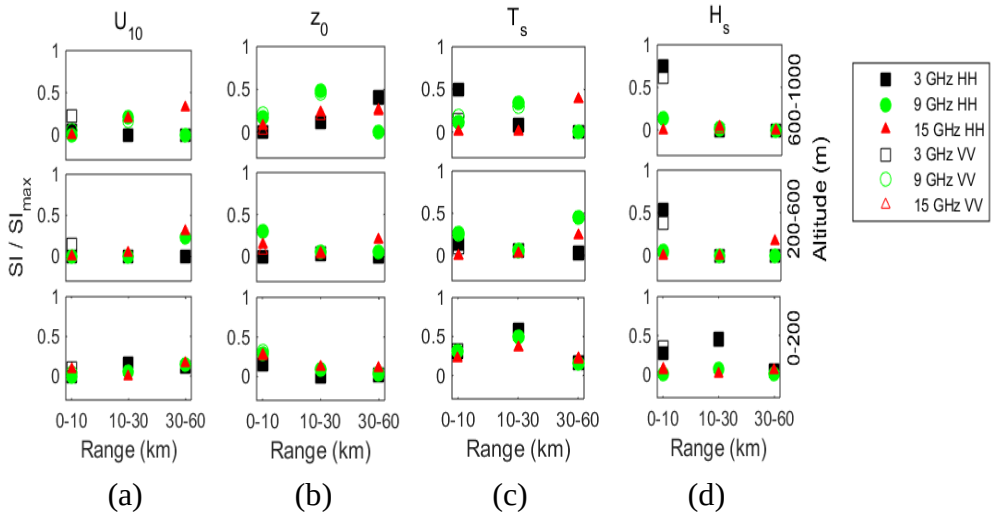

Figure 23: Normalized *SI* by region for roughness parameters: (a) U_{10}, (b) z_0, (c) T_s, and (d) H_s.

5.0 Conclusions

This study calculates global sensitivity of radar wave propagation to MABL environmental parameters using the EFAST sensitivity method and VTRPE propagation simulation. Results show that there are significant interaction effects that need consideration to correctly assess the importance of a given environmental parameter. These interactions are evident because *TSI* is generally much higher than *SI*, where the latter only considers leading order effects. Sensitivity varies more with radar frequency than polarization, which has little impact on the relative importance of the parameters. Atmospheric parameters are more important than ocean surface parameters, indicating that atmospheric refraction has a greater influence on propagation than reflection and scattering effects from the sea surface.

For the atmosphere, the mixed layer generally has the strongest leading order (*SI*) and total order (*TSI*) effect on propagation (Figure 11). Overall, the mixed layer height, h_{ML}, is the most important parameter, likely because of the strong role it plays in determining the vertical refractive structure of the atmosphere. The relative importance of mixed layer height increases with frequency.

For the sea surface, roughness parameters are generally the most important, except at 3 GHz, where directionality dominates (Figure 11). As frequency increases, a greater number of sea surface parameters affect propagation and their sensitivity values tend to

increase. Swell period is the most consistently important ocean surface parameter, primarily due to its interaction effects, despite not being the top ranking ocean surface parameter overall at every frequency (Figure 11).

The relative importance of the parameters varies with location and frequency. Figure 24 summarizes the top atmospheric, sea surface, and overall parameter in each region. Variation in the top parameter with frequency increases with altitude. That is, high altitude regions have different top parameters for each frequency, while there is the most frequency overlap in top rank at the low altitude regions. In all regions except the high altitude long-range region, the top atmospheric parameter is the top parameter overall (Figure 24; top right region). In this region, farthest from the transmitter, wind speed, U_{10}, is the top parameter at 9 and 15 GHz almost entirely due to interactions. At these frequencies, wind speed has substantial effects on propagation at high altitude mid-to-long range. Swell direction (θ_s) is also important at mid-to-high altitude at low frequency (3 GHz). At low altitude mid-range, wind direction (θ_w) is the top ocean surface parameter at 3 and 9 GHz. Thus, with regard to directionality and wind speed, as altitude increases, the most frequently occurring top ocean surface parameter goes from wind direction to swell direction to wind speed when considering all frequencies together. Swell period, T_s, is the top ocean surface parameter in three regions for at least one frequency. In many of the other regions, T_s is a close second, which suggests that it is a highly influential ocean surface parameter overall. However, sea surface salinity, *SSS*, is the top ranked ocean surface parameter in six regions a total of ten times (at different frequencies), again mostly due to interaction effects. Swell height, H_s, is a significant factor at short range (except at low altitude) for lower frequencies, and has some

polarization dependence. While polarization plays a small role overall, its chief effects are seen in the sensitivity of some ocean surface parameters at short range (Figure 24). Because the reflection and scattering behavior off the sea surface can be affected by polarization, it is reasonable that the sensitivity of a strong dielectric property of the surface (*SSS*) and H_s are dependent on polarization.

For the atmosphere, the evaporation duct height, z_d, is certainly the most important parameter near the transmitter (Figure 24), consistent with prior studies. Its importance diminishes with range and altitude at a rate that is frequency dependent; this frequency dependence is most clear for range. The mixed layer height, h_{ML}, and refractivity gradient, m_{ML}, dominate nearly all regions, except nearest and farthest from the transmitter. Inversion layer strength, ΔM, has a particularly high degree of interaction at 3 GHz, making it the top parameter at high altitude, except at short range. Because the inversion layer occurs in the mid-altitude regions most of the time in this study and lower frequency radar signals leak through ducts more easily than higher frequency signals, the high *TSI* of ΔM at 3 GHz in this upper layer suggests that duct leakage plays an important role on path loss at these altitudes.

The rough surface, turbulence, and transfer of heat, momentum, and energy in the MABL can cause significant effects on radar wave propagation, compromising the accuracy and predictability of the performance of radar systems. Figure 24 serves as a spatial map of the importance of environmental parameters with regard to propagation in the MABL. Although the study does not address physical causes for variations in the refractivity profile, it certainly highlights what aspects of the refractivity profile are most important and consequently, aids in determining what physical mechanisms ought to be focused on

with respect to their impact on the refractivity profile for various applications. Also, this study is limited by using only range independent *M*-profiles, which can lead to radar propagation prediction errors (Doggett, 1997; Gerstoft, 2003). Future work should incorporate range dependent *M*-profiles to further assess the relative importance of the horizontal spatial variability of the refraction profile relative to the sensitivities of the vertical structure examined in this study. Another limitation of this study is the independent variation of the aerodynamic roughness height, z_0, from the sea surface roughness parameters. Although, similar trends are observed for wind speed and z_0. Clearly, a more rigorous treatment of the aerodynamic roughness would be to couple it with the ocean roughness parameters, and this should be considered in future studies. Finally, use of the mathematically based stacked model (in combination with the EFAST method) can result in unrealistic sudden changes in the vertical profile that are likely to be sharper than those observed in the natural environment. It is possible that such unrealistic sudden changes artificially increase the sensitivity of *PL* to the mixed layer and upper *M*-gradients. To overcome these limitations, future work should consider smoothing such parametric profiles to make them more consistent with observations in the natural environment.

The regional and whole domain sensitivity results can be used to guide future modeling (forward and inverse) studies to help target the most important sea surface and atmospheric refractivity parameters to be predicted from NWP and RFC studies. Conversely, which parameters are not significant can be treated minimally. Measurement campaigns can also utilize these results, particularly those aimed towards radar wave propagation simulation validation. These sensitivity results can be used to help guide

what environment aspects need to be characterized at high resolution during such campaigns to enable better comparisons between measurements and models, and, on the other hand, what environmental measurements are unnecessary. Furthermore, the results of this study can be validated experimentally by making comparisons between modeled and measured propagation using various resolutions of environmental measurements. For example, if the parameters deemed of highest and lowest importance are prescribed at high accuracy versus low accuracy, is the model-versus-measurement comparison impacted in a manner consistent with the findings of this study?

Finally, this study is limited to low grazing angle ship/platform based radars with a csc^2 beam pattern at 3-15 GHz frequencies. The methodology laid out in this study for examining the sensitivity of the propagation could be performed for different system configurations, such as air-borne antennas with other radiation patterns at high grazing angles. Moreover, this sensitivity analysis approach can also be used to evaluate environmental effects on other remote sensors, such as infrared (IR), optical, and acoustic sensors.

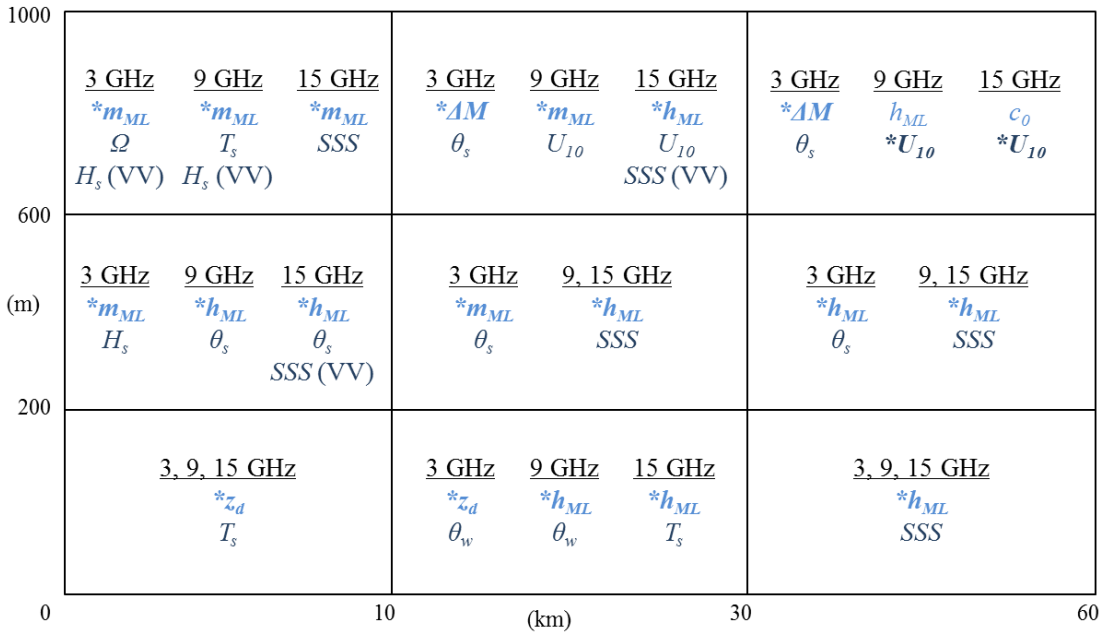

Figure 24: Chart illustrating the top atmospheric (light blue) and ocean surface (dark blue) parameter for each region at all frequencies, shown for HH polarization and ranked by *TSI*. If there is a discrepancy between polarizations, the VV value is also noted. The top overall parameter in each region is bold with an asterisk. Axes are not to scale.

6.0 References

Anderson, K.D. (1989), Radar measurements at 16.5 GHz in the oceanic evaporation duct, *IEEE Trans. Antennas Propag.*, 37(1), 100-106.

Apel, J.R. (1994), An improved model of the ocean surface wave vector spectrum and its effects on radar backscatter, *J. Geophys. Res.*, 99(C8), 16269-16291.

Babin, S.M., G.S. Young, and J.A. Carton. (1996), A new model of the oceanic evaporation duct, *J. Appl. Meteorol.*, 36, 193-204.

Battan, L.J. (1973), *Radar Observation of the Atmosphere*, University of Chicago Press, 324 pp.

Bean, B.R., and Dutton, E.J. (1968), *Radio Meteorology, 1st Ed.*, New York, Dover, 435 pp.

Benhmammouch, O., N. Caouren, and A. Khenchaf. (2009), Influence of sea surface roughness on electromagnetic waves propagation in presence of evaporation duct, *Proceedings of International Radar Conference*, 12-16 Oct., Bordeaux, France.

Bowditch, N. (2002), U.S. National Imagery and Mapping Agency, *The American Practical Navigator: An Epitome of Navigation*, Washington: Government Printing Office (Pub. No. 9).

Burk, S.D., and W.T. Thompson. (1997), Mesoscale modeling of summertime refractive conditions in the Southern California Bight, *J. Appl. Meteorol.*, 36, 22-31.

Chang, H.T. (1971), The effect of tropospheric layer structures on long-range VHF radio propagation, *IEEE Trans. Ant. Propag.*, 19(6), 751-756.

Coulman, C.E. (1991), Tropospheric phenomena responsible for anomalous refraction at radio wavelengths, *Astron. and Astrophys.*, 251, 743-750.

Craig, K.H., and M.F. Levy. (1991), Parabolic equation modeling of the effects of multipath and ducting on radar systems, *IEEE Proc.*, 138(2), 153-162.

Cukier, R. I., C. M. Fortuin, K. E. Shuler, A. G. Petschek, and J. H. Schaibly. (1973), Study of the sensitivity of coupled reaction systems to uncertainties in rate coefficients. I Theory, *J. Chem. Phys.*, 59, 3873-3878.

Cukier, R.I., J.H. Schaibly, and K.E. Shuler. (1975), Study of the sensitivity of coupled reaction systems to uncertainties in rate coefficients. III. Analysis of the approximations, *J. Chem. Phys.*, 63, 1140-1149.

Cukier, R.I., H.B. Levine, and K.E. Shuler. (1978), Nonlinear sensitivity analysis of multiparameter model systems, *J. Comput. Phys.*, 26, 1-42.

Doggett, M.K. (1997), An atmospheric sensitivity and validation study of the variable terrain radio parabolic equation model (VTRPE), *97M-04*, Air Force Institute of Technology, Ohio.

Dougherty, H.T., and B.A. Hart. (1979), Recent progress in duct propagation predictions, *IEEE Trans. Ant. Propag.*, AP-27(4), 542-548.

Dresp, M.R., and A.S. Ratner. (1977), Tropospheric duct propagation beyond the horizon at UHF, *Int. Union Radio Sci. Bulletin*, 31-36.

Ekstrom, P.A. (2005), Eikos: A simulation toolbox for sensitivity analysis, *Degree Project*, Uppsala Universitet, Sweden.

Falcone Jr., V.J., and R. Dyer. (1985), Electromagnetic Wave Propagation in the Lower Atmosphere, *Handbook of Geophysics and the Space Environment*, A.S. Jursa, Ed., Air Force Geophysics Laboratory, Air Force Systems Command, U.S. Air Force, Hanscom Air Force Base, Mass.

Fishback, W.T., and P.J. Rubenstein. (1944), Further measurements of 3- and 10-cm reflection coefficients of sea water at small grazing angles, *RL Report No. 568*.

Freehafer, J.E., W.T. Fishback, W.H. Furry, and D.E. Kerr. (1951), *Propagation of Short Radio Waves*, McGraw-Hill, London, 728 pp.

Friis, HT. (1946), A note on a simple transmission formula, *Proc. IRE*, 34, 254-256.

Gerstoft, P., L.T. Rogers, J.L. Krolik, and W.S. Hodgkiss. (2003), Inversion for refractivity parameters from radar sea clutter, *Radio Sci.*, 38(3), 8053.

Goldstein, H. (1951), Sea Echo, *Propagation of Short Radio Waves*, D.E. Kerr, Ed., McGraw-Hill, New York, 728 pp.

Gossard, E.E. (1981), Clear weather meteorological effects on propagations at frequencies above 1 GHz, *Radio Sci.*, 16(5), 589-608.

Griffiths, D.J. (1998), *Introduction to Electrodynamics, 3rd Ed.*, Prentice-Hall, New Jersey, 576 pp.

Gunashekar, S.D., E.M. Warrington, D.R. Siddle, and P. Valtr. (2007), Signal strength variations at 2 GHz for three sea paths in the British Channel Islands: Detailed discussion and propagation modeling, *Radio Sci.*, 4020, 1-13.

Gunn, K.L.S., and T.W.R. East. (1954), The microwave properties of precipitation particles, *Q.J.R. Meteorol. Soc.*, 80, 522-545.

Haack, T., W. Changgui, S. Garrett, A. Glazer, J. Mailhot, and R. Marshall. (2010), Mesoscale modeling of boundary layer refractivity and atmospheric ducting. *J. Appl. Meteorol. & Clim.* 49, 2437-2457.

Hitney, H.V., and L.R. Hitney. (1990), Frequency diversity effects of evaporation duct propagation, *IEEE Trans. Ant. Propag.*, 38(10), 1694-1700.

Hitney, H.V., R.A. Pappert, and C.P. Hattan. (1978), Evaporation duct influences on beyond-the-horizon high altitude signals, *Radio Sci.*, 13(4), 669-675.

Hitney, H.V., J.H. Richter, R.A. Pappert, K.D. Anderson, and G.B. Baumgartner, Jr. (1985), Tropospheric radio propagation assessment, *Proc. IEEE*, 73(2), 265-283.

Hitney, H.V., and R. Veith. (1990), Statistical assessment of evaporation duct propagation, *IEEE Trans. Ant. Propag.*, 38(6), 794-799.

Ivanov, V.K., V.N. Shalyapin, and Yu. V. Levadny. (2009), Microwave scattering by tropospheric fluctuations in an evaporation duct, *Radiophys. Quantum Electr.*, 52(4), 277-286.

Jansen, M.J.W., W.A.H. Rossing, and R.A. Daamen. (1994), Monte Carlo estimations of uncertainty contributions from several independent multivariate sources, *Predictability and Nonlinear Modeling in Natural Sciences and Economics*, Springer, Netherlands.

Jeske, H. (1973), State and limits of prediction methods of radar wave propagation conditions over sea, *Modern topics in microwave propagation and air-sea interaction*, A. Zancla, Ed., Springer, Netherlands, 130-148.

Johnson, J.T., R.T. Shin, J.A. Kong, L. Tsang, and K. Pak. (1998), A numerical study of the composite surface model for ocean backscattering, *IEEE Trans. Geosci. Remote Sens.*, 36(1), 72-83.

Karasawa, Y., T. Matsudo, and T. Shiokawa. (1990), Wave height and frequency dependence of multipath fading due to sea reflection in maritime satellite communications, *Electron. Comm. Jpn. 1*, 73(1), 95-106.

Karimian, A., C. Yardim, P. Gerstoft, W.S. Hodgkiss, and A.E. Barrios. (2011), Refractivity estimation from sea clutter: An invited review, *Radio Sci.*, 46, RS6013.

Karimian, A., C. Yardim, T. Haack, P. Gerstoft, W.S. Hodgkiss, and T. Rogers. (2013), Toward the assimilation of the atmospheric surface layer using numerical weather prediction and radar clutter observations, *J. Appl. Meteorol.*, 52(10), 2345-2355.

Kerr, D.E. (1951), Tropospheric refraction, *Propagation of Short Radio Waves*, D.E. Kerr, Ed., McGraw-Hill, New York, 728 pp.

Kerr, D.E., J.E. Freehafer, W.T. Fishback, and W.H. Furry. (1951), Theory of Propagation in a Horizontally Stratified Atmosphere, *Propagation of Short Radio Waves*, D.E. Kerr, Ed., McGraw-Hill, New York, 728 pp.

Kerr, D.E., W.T. Fishback, and H. Goldstein. (1951), Reflections from the Earth's Surface, *Propagation of Short Radio Waves*, D.E. Kerr, Ed., McGraw-Hill, New York, 728 pp.

Koda, M., G.J. McRae, and J.H.M. Seinfeld. (1979), Automatic sensitivity analysis of kinetic mechanisms, *Int. J. Chem. Kinet.*, 11, 427-444.

Kukushkin, A. (2004), *Radio Wave Propagation in the Marine Boundary Layer*, John Wiley & Sons, 204 pp.

Marino, S., I.B. Hogue, C.J. Ray, and D.E. Kirschner. (2008), A methodology for performing global uncertainty and sensitivity analysis in systems biology, *J. Theor. Biol.*, 254, 178-196.

Morris, M.D. (1991), Factorial Sampling Plans for Preliminary Computational Experiments, *Technometrics*, 33, 161-174.

O'Donnell, R. (2007), Introduction to Radar Systems. *MIT OpenCourseWare: Massachusetts Institute of Technology*, http://ocw.mit.edu/resources/res-ll-001-introduction-to-radar-systems-spring-2007 (Sep 4, 2013).

Pappert, R.A., and C.L. Goodhart. (1977), Case study of beyond-the-horizon propagation in tropospheric duct environments, *Radio Sci.*, 12(1), 75-87.

Paulus, R. A. (1984), Practical application of the IREPS evaporation duct model, *NOSC TR*, 966, 29, Naval Ocean Systems Center, San Diego, Calif., 71 pp.

Paulus, R. A. (1985), Practical application of an evaporation duct model, *Radio Sci.*, 20(4), 887-896.

Paulus, A. (1989), Specification for evaporation duct height calculations, *No. NOSC/TD-1596*, Naval Ocean Systems Center, San Diego, CA, 35 pp.

Paulus, R.A. (1990), Evaporation duct effects on sea clutter, *IEEE Trans. Ant. Propag.*, 38(11), 1765-1771.

Paulus, R.A. (1994), VOCAR: An experiment in variability of coastal atmospheric refractivity, *Proc. IGARSS*, 1, 386-388.

Reddy, R. G., and B.M. Reddy. (2007), Sea breeze signatures on line-of-sight microwave links in tropical coastal areas, *Radio Sci.*, 42, RS4021, 1-13.

Rotheram, S. (1974), Radiowave propagation in the evaporation duct, *Marconi Review*, 37(192), 18-40.

Ruthroff, C.L. (1971), Multiple-path fading on line-of-sight microwave radio systems as a function of path length and frequency, *Bell Syst. Tech. J.*, 50(7), 2375-2398.

Ryan, F. (1991), Analysis of electromagnetic propagation over variable terrain using the parabolic wave equation, *TR1453*, Naval Ocean Systems Center, San Diego, Calif. 38 pp.

Saltelli, A., S. Tarantola, and F. Campolongo. (2000), Sensitivity analysis as an ingredient of modeling, *Stat. Sci.*, 15, 377-395.

Saltelli, A., S. Tarantola, and K.P.-S. Chan, (1999), A quantitative model-independent method for global sensitivity analysis of model output, *Technometrics*, 41, 39-56.

Schaibly, J.H., and K.E. Shuler. (1973), Study of the sensitivity of coupled reaction systems to uncertainties in rate coefficients. Part 2. Applications, *J. Chem. Phys.*, 59, 3879-3888.

Sirkova, I. (2012), Brief review on PE method application to propagation channel modeling in sea environment, *Cent. Eur. J. Eng.*, 2(1), 19-38.

Sirkova, I., and M. Mikhalev. (2003), Influence of tropospheric duct parameters changes on microwave path loss, *Microwave Review*, 9(2), 43-46.

Skolnik, M. I. (1990), *Radar Handbook*, McGraw-Hill, New York, 1200 pp.

Sobol, I.M. (1993), Sensitivity estimates for nonlinear mathematical models, *Math. Modeling and Computational Experiment*, 1, 407-414.

Sobol, I.M. (2001), Global sensitivity indices for nonlinear mathematical models and their Monte Carlo estimates, *Math. Comput. Simulat.*, 55, 271-280.

Stephansen, E.T. (1981), Clear-air propagation on line-of-sight radio paths: A review, *Radio Sci.*, 16(5), 609-629.

Stephansen, E.T., and G.E. Mogensen. (1979), Experimental investigation of some effects of multipath propagation on a line-of-sight path at 14 GHz, *IEEE Trans. Commun.*, 27(3), 643-647.

Turton, J.D., D.A. Bennetts, and S.F.G. Farmer. (1988), An introduction to radio ducting, *Meteorol. Mag.*, 117, 245-254.

Van Vleck, J.H. (1947a), The absorption of microwaves by oxygen, *Phys. Rev.*, 71, 413-424.

Van Vleck, J.H. (1947b), The absorption of microwaves by uncondensed water vapor, *Phys. Rev.*, 71, 425-433.

Wait, J.R., and K.P. Spies. (1969), Internal guiding of microwaves by an elevated tropospheric layer, *Radio Sci.*, 4(4), 319-326.

Wetzel, L.B. (1990), Sea Clutter, *Radar Handbook*, M.I. Skolnik, Ed., McGraw-Hill, New York, 1200 pp.

Wolff, C., (2009), *Radar Tutorial*, http://www.radartutorial.eu/01.basics/rb02.en.html